Journal of Materials Chemistry A

ROYAL SOCIETY OF CHEMISTRY

PERSPECTIVE

View Article Online
View Journal | View Issue

Cite this: J. Mater. Chem. A, 2023, 11, 16933

2D transition metal-based phospho-chalcogenides and their applications in photocatalytic and electrocatalytic hydrogen evolution reactions

K. Pramoda*[a] and C. N. R. Rao *[b]

Received 17th March 2023
Accepted 30th June 2023

DOI: 10.1039/d3ta01629c

rsc.li/materials-a

The utilization of hydrogen (H_2) as a renewable substitute for fossil fuel can mitigate issues related to energy shortage and associated global warming. The generation of H_2 *via* water splitting by photo and electrocatalytic means is of significant importance. The employment of a semiconductor catalyst reduces the high energy barrier (237 kJ mol^{-1}) associated with a water-splitting reaction to yield H_2 and O_2. Sustainable H_2 production demands the utilization of noble-metal-free, efficient, and stable catalysts over a wide pH range. In recent times, layered transition metal thio(seleno) phosphates (MPX_3, X = S, Se) are reported to be highly efficient for H_2 evolution reaction owing to their earth-abundance, rich active sites, wide spanned band gap of 1.2 to 3.5 eV, and high chemical stability. In this perspective, advances in 2D monometallic and bimetallic MPX_3 compounds are reviewed comprehensively from the viewpoint of water splitting, especially the hydrogen evolution reaction (HER). This study includes the composition, structural engineering, heterostructure, and hierarchically structural design in enhancing the HER activity of MPX_3. Computational results providing insights into the intrinsic photo and electrocatalytic HER activity of 2D MPX_3 are presented. Finally, the challenges and opportunities in further improving MPX_3 activity towards HER and associated catalysis reactions are discussed.

1. Introduction

The massive utilization of non-renewable fossil fuels to meet ever-increasing global energy requirements is leading to fuel scarcity and CO_2 emission at an alarming rate gives rise to global warming.[1–8] Therefore, establishing global-scale, renewable, efficient, and carbon-free emission combined fuel-combustion technology is of significant importance.[1–4] Fuel cell technology is an environmentally-safe route of generating energy than the other existing methods.[5–7] The fuel cell utilizing hydrogen (H_2) and oxygen (O_2) as fuels at the anode and cathode, respectively, will be the suitable one amongst the numerous types of fuel cells because it gives only water (H_2O) as the product.[8–10] The main goal is to generate H_2 from renewable sources, ideally H_2O. Water can be decomposed into H_2 and O_2 through photochemical, electrochemical, and photo-electrochemical strategies by utilizing solar, electrical energy, and a combination of solar-electricity energy, respectively.[11–14,19] The main challenge is to generate H_2 from renewable sources, preferably H_2O. But, water splitting $\left(2H_2O \rightarrow H_2 + \frac{1}{2}O_2\right)$ is thermodynamically an uphill reaction that involves a large Gibbs free energy change of 237 kJ mol^{-1}.[15–18] With the help of an appropriate catalyst one can decrease the energy barrier for water splitting and increase the H_2 evolution rate. Platinum or platinum group materials (PGMs) are regarded as the best catalysts for electrochemical H_2 evolution reaction (HER).[20–22] However, high-cost, stability issues under various electrochemical conditions and intolerance to catalytic poisoning severely limit their applicability as HER catalysts. In the last decade, there is a major thrust into exploiting low-cost, earth-abundant, and stable catalysts, particularly the non-precious metal catalysts.[23–26] Therefore, non-noble 2D metal catalysts, such as transition metal chalcogenides (TMDCs),[27–30] carbides,[31] nitrides,[32] and phosphides,[33] have been investigated for the potential replacement of the noble metal catalysts for water splitting owing to their fascinating optical and electrical properties. It has been reported that the bulk MoS_2 is inactive for the hydrogen evolution reaction (HER), whereas, mono or few-layer MoS_2 shows excellent HER performance.[34,35] The incorporation of Co and Ni into the MoS_2 matrix was reported to enhance the electrocatalytic activity significantly.[36–38] While alloy phases, MoS_xSe_{1-x}, wherein Se in combination with S, permit tuning of HER activity.[39,40]

Akin to TMDCs, 2D transition metal phosphides (TMPs) are reported to show bifunctional properties as HER and oxygen evolution reaction (OER) catalysts and also display long-term stability in a wide pH range.[41–44] Theoretically, it is predicted

[a]Centre for Nano and Material Sciences, Jain (Deemed-to-be University), Jain Global Campus, Kanakapura, Bangalore, Karnataka, 562112, India

[b]New Chemistry Unit, School of Advanced Materials and International Centre for Material Science, Jawaharlal Nehru Centre for Advanced Scientific Research (JNCASR), Jakkur P. O., Bengaluru, 560064, India. E-mail: cnrrao@jncasr.ac.in

that the phosphorous atom of TMPs acts as an active site for intermediate hydrogen adsorption and desorption during water splitting. Jia *et al.*[45] compared the Gibbs free energy change (ΔG_{H^*}) of hydrogen adsorbed, which is a main intermediate state in HER, on to the different active sites MoP, MoS_2, and Mo_2C catalysts by density functional theory (DFT) calculations (Fig. 1a and b). According to the Sabatier principle, too strong or too weak adsorption is not favorable for the water reduction reaction. The ΔG_{H^*} values for Mo-terminated MoP, MoS_2, and Mo_2C were calculated as 0.16, 0.19, and 0.24 eV, respectively. These results indicate that the P atom in MoP plays the equivalent role as S of MoS_2 and C in Mo_2C. Further, a subtle smaller ΔG_{H^*} value for MoP as compared to MoS_2 and Mo_2C, indicates that MoP possesses higher catalytic activity. In another study, Miguel *et al.*[46] using DFT calculations demonstrated that the ternary pyrite-type cobalt phosphosulfide can be an efficient catalyst for both photocatalytic and electrocatalytic HER since the cobalt octahedra contain more-electron donating P^{2-} sites compared to S^{2-}, owing to thermoneutral H^+ adsorption at the active sites. The cubic crystal structure of CoPS can be envisaged as Co^{3+} octahedra surrounded by dumbbells with a uniform arrangement of P^{2-} and S^{2-} ligands (Fig. 1c and d). Further, DFT calculations revealed that ΔG_{H^*} on the (100) surface of CoPS at the Co site is more favorable compared to the CoS_2 constituent. As shown in Fig. 1f–i, after spontaneous adsorption of H^+ at open P sites, adjacent Co^{3+} atoms are reduced to Co^{2+}, which brings ΔG_{H^*} value for cobalt near the thermoneutral value. Subsequent H^+ adsorption at Co^{2+} sites induces the oxidation of Co^{2+} to Co^{3+} as shown in Fig. 1f–i. Such synergistic interaction is not realized in the case of CoS_2 since Co^{3+} sites are energetically more favorable for H^+ adsorption than open S^{2-} ligands. In addition, Miguel *et al.*[46] showed that CoPS nanostructures display electrocatalytic HER activity comparable to the Pt/C catalyst with a current density of 10 mA cm^{-2} at an overpotential as low as 48 mV and also shows exceptional stability. The Pt/C-like HER activity of CoPS inspired other researchers to study MPX_3 systems containing Mn, Fe, Ni, Cd, *etc.* metals. But, some of the 2D family MPX_3 systems such as $MnPS_3$, $FePS_3$, and $NiPS_3$ showed marginal electrocatalytic H_2 evolution activity due to low intrinsic electronic conductivity.[47] Coupling of MPX_3 with conducting graphene[47] and doping of Co into $MnPS_3$ and $NiPS_3$ structures was reported to improve HER activity.[48,49] Doping modifies the valence band and conduction edges and improves the electron transport rate. Further, MoS_2

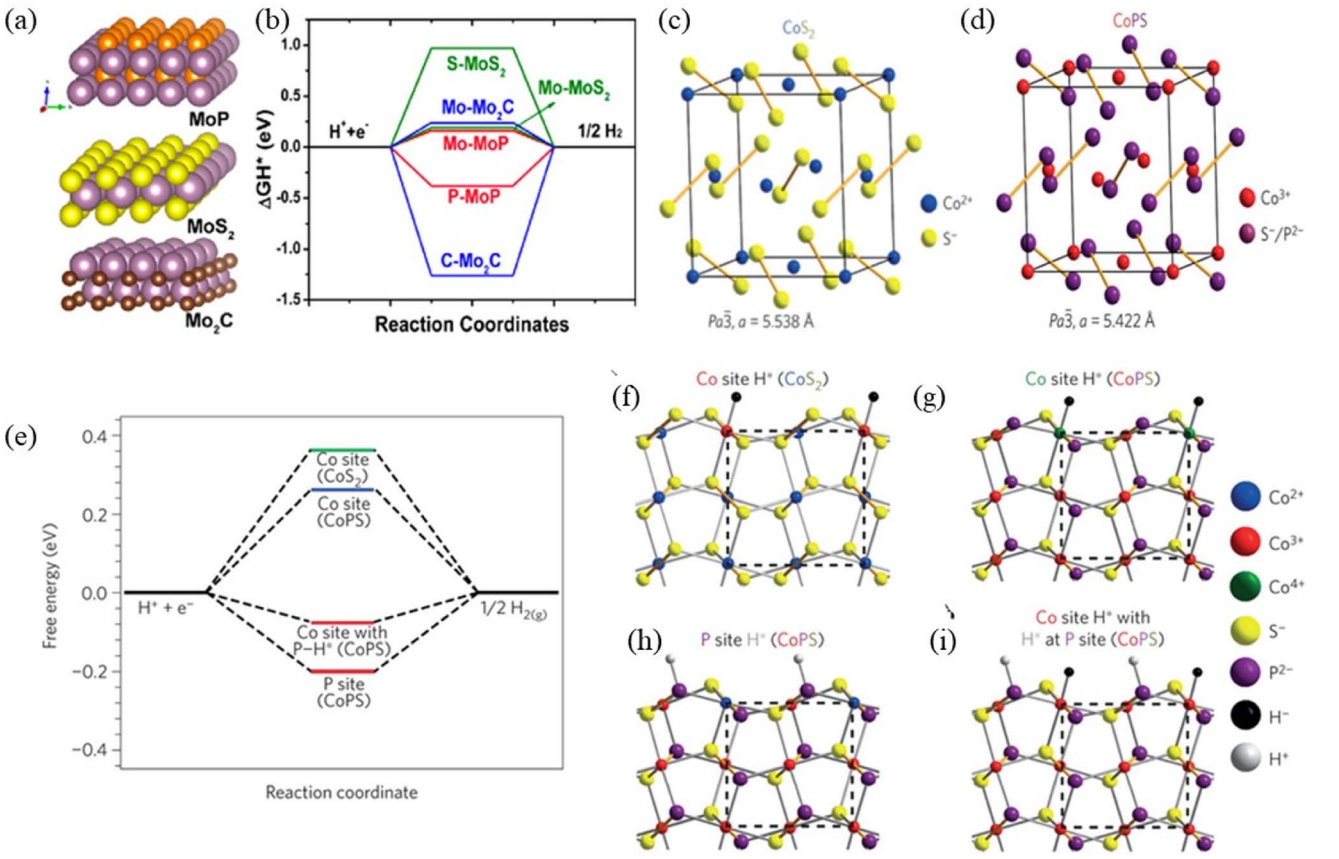

Fig. 1 (a) Schematic depiction of the layered structure of 2D molybdenum phosphide (MoP), molybdenum disulfide (MoS_2), and molybdenum carbide (Mo_2C). (b) Gibbs free energy diagram of the H_2 evolution for MoP, MoS_2, and Mo_2C at different sites. Reprinted with permission.[45] Copyright 2017, American Chemical Society. (c and d) Crystal structures of CoS_2 and CoPS systems. (e) Free energy diagrams of the H_2 evolution for CoS_2 and CoPS at different sites. Structural demonstration of hydrogen adsorption (H*) at the Co site on (100) plane of CoS_2 (f), at the Co site (g), P site (h), and at the P site after H* at the Co site (i) on (100) plane of CoPS. Reprinted with permission. Copyright 2015, Springer nature.[46]

in combination with MPX_3 facilitates hydrogen spillover during HER from MoS_2 edge sites to TMPCs.[50,51]

As discussed in prior sections, water splitting is thermodynamically energy-intensive as it demands a relatively large free energy of 237 kJ mol^{-1} to produce one mole of H_2 and O_2 each.[15,19] To overcome this large energy barrier, researchers are utilizing semiconductor photocatalysts for water splitting, which can mimic the natural photosynthesis process involving the following two half-reactions.[52,53]

$$\text{Water reduction: } 2H^+ + 2e^- \rightarrow H_2,\ \Delta E^o = -0.41\ \text{V}$$

$$\text{Water oxidation: } 2H_2O \rightarrow O_2 + 4H^+ + 4e^-,\ \Delta E^o = +0.82\ \text{V}$$

$$\text{Overall water splitting}: 2H_2O_{(l)} \rightarrow H_{2(g)} + \frac{1}{2}O_{2(g)},\ \Delta E^o = +1.23\ \text{V},\ \Delta G^o = +237\ \text{kJ mol}^{-1}$$

The high Gibbs free energy barrier for water redox reactions can be reduced by employing semiconductors as photocatalysts and, therefore, the H_2 evolution rate can be improved. The standard reduction potentials for H^+/H_2 reduction and oxidation potential for H_2O/O_2 are estimated to be −0.41 and +0.82 V (*vs.* NHE), respectively. To achieve overall water splitting by utilizing a semiconductor, the conduction band minimum (CBM) energy of the semiconductor should be higher than the H^+/H_2 reduction potential and its valence band maximum (VBM) energy must be lower than the H_2O/O_2 oxidation potential.[54–56] The water splitting utilizing semiconductor photocatalyst comprises three essential steps: (1) absorption of solar energy by the semiconductor; (2) generation and mobilization of electron–hole pair from bulk to the active sites of the semiconductor; (3) water reduction (H^+/H_2) and oxidation (H_2O/O_2) reactions by photogenerated electron and hole pair at the conduction band (CB) and valence band (VB) of the semiconductor, respectively (Fig. 2). As shown in Fig. 2a and b, water splitting using semiconductors could be a one-step or two-step approach based on whether a single component is utilized or a combination of two or more semiconductor systems. The one-step route involves the photoexcitation of the semiconductor and water reduction and oxidation reaction by the electron and holes at the CB and VB of the semiconductor. While the two-step method includes concomitant photoexcitation of two semiconductors, hydrogen (H^+/H_2) and oxygen (H_2O/O_2) evolution occurs individually at different semiconductors similar to the usual Z-scheme photosynthesis.

In 1972, Fujishima *et al.*[57] primarily described the use of TiO_2 electrodes as photocatalysts for water-splitting reactions, since then, numerous semiconductors such as ZnO, Sb_2O_3, WO_3, and TiO_2 have been utilized as photocalaysts.[58,59] However, the utilization of semiconductor photocatalyst requires the use of noble-metal cocatalysts in combination to realize higher water splitting efficiency.[60,61] Hence, researchers are relentlessly exploring non-noble metal catalysts for water splitting to make the process cost-effective. In this regard, 2D materials such as metal nitrides, carbides, and phosphides have been explored as proficient catalysts for water reduction reactions. As discussed earlier, photon absorption, electron–hole pair separation and water redox reactions at the catalyst active sites are three crucial stages in photocatalytic water splitting. 2D material band gap can be modified by varying the number of stacked sheets, which fulfills the first condition. Secondly, due to the atomic thickness of 2D material, photogenerated charge-carriers have to cover lesser distances to reach the surface energetic sites. Further, the high specific surface area of 2D materials provides abundant active sites and higher accessibility for H^+ adsorption. Lately, Ida *et al.*[62] demonstrated how solar flux density and charge carrier lifetime in 0D nanocrystals and 2D crystal affects the water-splitting process (Fig. 3). A nanocrystal requires four excited electrons to ensure complete water splitting. But, photogenerated charge carriers possess a very short average lifetime of 1 μs before recombination. Therefore, to harvest four electrons, the nanocrystal should absorb four photons within a shorter period of 1 μs time. The solar flux density in the Earth's atmosphere is estimated to be 2000 μmol s^{-1} m^{-2}. Thus, 4 ms is essential for photons to get adsorbed by the 0D nanocrystal and it is tough to afford such high solar flux to achieve water splitting using 0D nanocrystal. 2D materials, on the other hand, could minimize recombination rate by providing shorter pathways for charge-carriers to reach the active sites, thereby low solar energy flux is paramount in the case of 2D materials to achieve water splitting.

2D transition metal thio(seleno) phosphates (MPX_3, X = S, Se) nanosheets containing Mn, Fe, Co, Ni, Cu, *etc.* metals have been investigated for photocatalytic HER due to their tunable composition, electronic structure, and wide band gap ranging from 1.3 to 3.5 eV.[63–65] The electronic structure and properties of the MPX_3 systems are investigated by optical absorption, photoluminescence, and DFT simulations. Zhang *et al.*[66] calculated the band structure of MPS_3 (M = Fe, Mn, Ni, Cd, Zn) and $MPSe_3$ (M = Fe, Mn) systems using the Heyd–Scuseria–Ernzerhof (HSE06) functional, which is presented in Fig. 4a–f. This study specifies that the band gap of single-layer MPX_3 varies from 1.90 to 3.44 eV, which surpasses the thermodynamic potential of 1.23 eV essential for water splitting. In addition, Yang *et al.*[67] calculated the dynamic stability of $MnPX_3$ (X = S or Se) nanosheets with the finite displacement method, and the corresponding phonon dispersion curve is shown in Fig. 4h and g. Interestingly, no imaginary phonon modes are observed in the phonon spectra, confirming the dynamic stability and they can be isolated as free-standing nanosheets. As displayed in the right panel of Fig. 4h and g, phonon bands below 8 THz are assigned to Mn–S/Se interactions, while the high frequency region above 8 THz corresponds to P_2X_6 moiety vibrations. Secondly, the radius of Se is greater than that of S, hence, the bond length of Mn–Se is larger than that of Mn–S and phonon bands of $MnSe_3$ are shifted towards low frequencies as compared to the $MnPS_3$ system.

Apart from the band gap, the valence band and conduction band edges must straddle with H^+/H_2 reduction and H_2O/O_2 oxidation potentials. Liu *et al.*[68,69] using HSE06 functional and partial density of states, calculated the orientation of CBM and

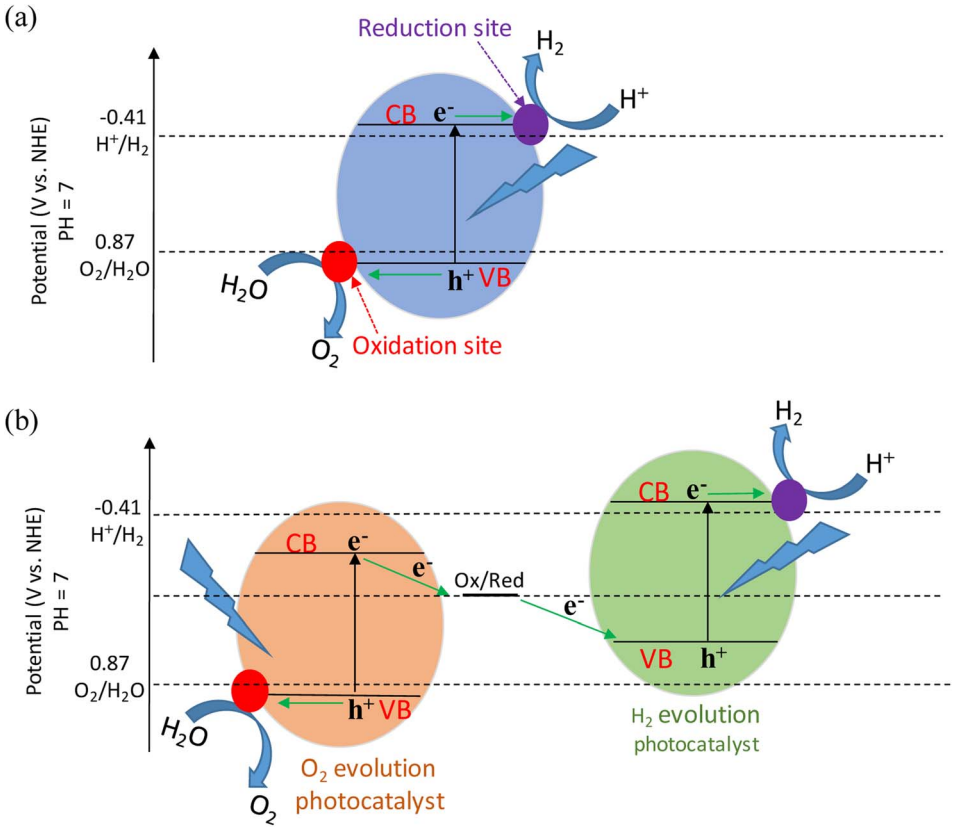

Fig. 2 Schematic of the function and essential role of semiconductor photocatalyst in decreasing the Gibbs free energy for water splitting reaction. (a and b) photocatalytic water splitting using a single-component or combination of two semiconductor systems.

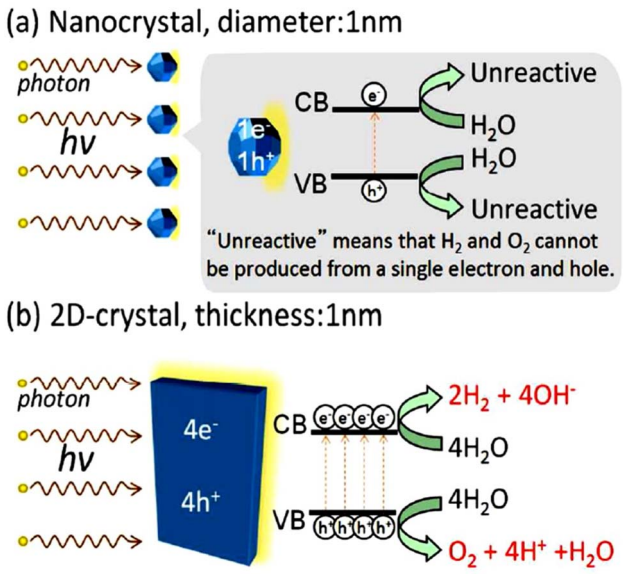

Fig. 3 Schematic illustration of the photocatalytic water redox reaction under solar light illumination for (a) 0D crystal and (b) 2D system. Replicated with the agreement.[62] Copyright 2014, American Chemical Society.

VBM edges relative to water redox potential (Fig. 5a). Further, Zhang *et al.*[66] by taking into consideration of stability of monolayered MPX_3 systems and variation in their redox potentials with changes in pH, calculated the band edges based on HSE06 functional studies (Fig. 5b). Among the studied materials, $FePSe_3$ displayed the narrowest band gap, which was further confirmed by optical absorption spectra as well. However, at pH = 7, $FePSe_3$ displayed a CBM edge lower than water reduction potential and hence it is not suitable for H^+/H_2 reduction. Therefore, a particular MPS_3 system can be chosen for either HER or OER based on the alignment of VBM and CBM edges relative to water redox potential. In addition, $MnPS_3$, $FePS_3$, and $NiPS_3$ displayed strong optical absorption in the visible range, which indicates their high capability to harvest visible light (Fig. 5c). These simulations have been experimentally verified by Du *et al.*[70] as well.

Strong visible light absorption characteristics and high carrier mobility (625.9 $cm^2\ V^{-1}\ s^{-1}$ for $MnPSe_3$) specify the MPX_3 system's potential capability for H_2 generation under solar light.[65,66,70] In addition, members of the MPX_3 family possess the aforementioned properties along with abundant phosphorous active sites for HER in mono or few-layer form; thus, it is realistic to assume that they can be good candidates for many catalysis reactions as non-precious metal catalysts. 2D $CdPS_3$ showed high HER performance of 10 880 μmol $h^{-1}\ g^{-1}$ while $MnPS_3$ and $FePS_3$ displayed 21.2 and 141.9 μmol $h^{-1}\ g^{-1}$, respectively, under solar light.[65,71,72] One drawback of 2D TMPCs is their weak oxidizing ability of the photogenerated holes because of the misaligned valence band maximum (VBM) edge for H_2O/O_2 oxidation potential and hence shows low stability

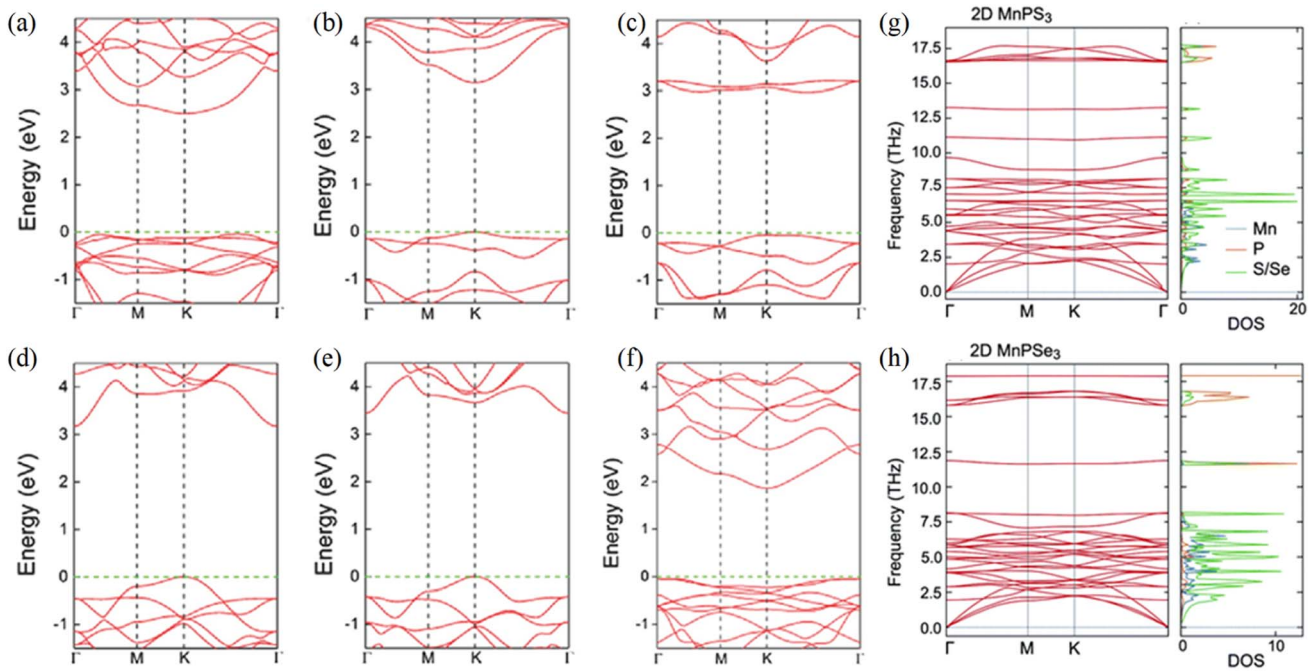

Fig. 4 Band structure near the Fermi level for (a) $FePS_3$, (b) $MnPS_3$, (c) $NiPS_3$, (d) $CdPS_3$, (e) $ZnPS_3$, and (f) $FePSe_3$ single-layers. Reprinted with permission.[66] Copyright 2018, Wiley publication. Phonon dispersion and the corresponding density of states for (g) $MnPS_3$ and (h) $MnPSe_3$ nanosheets. Reprinted with permission.[67] Copyright 2020, The Royal Society of Chemistry.

because of photocorrosion.[64,73] Combination of 2D MPX_3 with other $Cs_4W_{11}O_{35}$, CdS, TiO_2, and g-C_3N_4 nanostructures is reported to be beneficial for water splitting as latter systems possess strong hole oxidizing ability.

In this perspective, we provide an overview of various 2D TMPCs utilized for photocatalytic and electrocatalytic HER applications. The chemical vapor transport (CVT) method for bulk MPX_3 preparation is mentioned briefly and

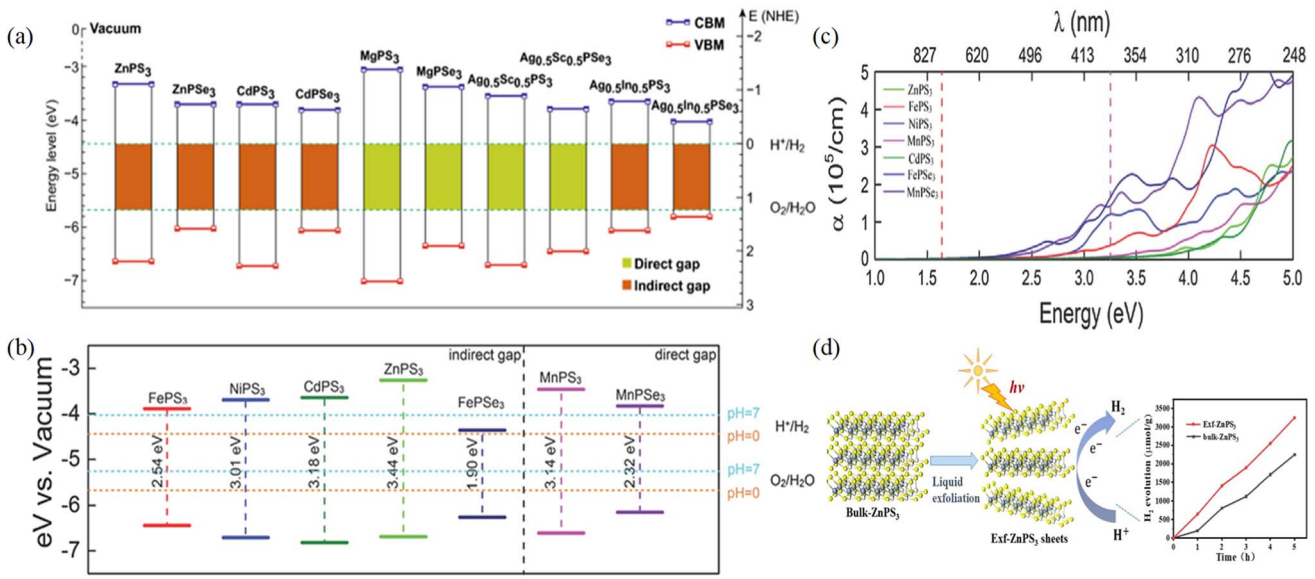

Fig. 5 (a) Band edge potential of mono-layered MPX_3 compounds. The energy scale is represented with respect to the normal hydrogen electrode (right *y*-axis) and vacuum level (left *y*-axis) in eV for reference. The redox potential of water is incorporated for assessment. Reproduced with permission.[68] Copyright 2001, Macmillan Publishers Ltd. (b) Location of VBM and CBM edge potentials of monolayer MPS_3 and $MPSe_3$ calculated using HSE06 functional. The redox potential of water at pH = 0 and pH = 7 is incorporated for comparison. (c) The optical absorption coefficient for MPS_3 compounds. The region between the red and purple lines indicates the visible range. Reprinted with permission.[66] Copyright 2018, Wiley publication. (d) Schematic shows that the exfoliated $ZnPS_3$ shows higher photocatalytic HER activity as compared to the bulk due to more exposed edge sites.[112]

micromechanical exfoliation and liquid-phase exfoliation approaches to prepare 2D MPX_3 from bulk crystal are discussed. The DFT approach demonstrating the significance of proper alignment of VBM and conduction band minimum (CBM) edges of 2D MPX_3 concerning water redox potential towards HER is discussed at length. To improve the catalytic activity of MPX_3, phase engineering, band structure engineering, and electronic state modulation by doping strategies have been employed (Fig. 6). Generation of the heterojunction between 2D MPX_3 with other $Cs_4W_{11}O_{35}$, CdS, TiO_2, and g-C_3N_4 nanostructures is reported to improve hole oxidizing ability. Further, photogenerated electrons are readily available for water reduction due to an in-built electric field gradient and therefore heterostructures are likely to display a higher HER rate and good stability. Besides, ferroelectric $CuInP_2S_6$ displays good HER characteristics and its activity can be further enhanced by coupling with other photocatalytically HER-active materials such as g-C_3N_4 and $ZnIn_2S_4$. The permanent polarization electric field and large exciton binding energy characteristics of ferroelectric $CuInP_2S_6$ induce spatial separation of the photogenerated carriers and reduction potential of electrons, respectively, thereby showing good H_2 evolution. Notably, the $CuInP_2S_6$/g-C_3N_4 heterostructure shows extraordinary stability under harsh photochemical conditions, suggesting its practical applicability.

2. Structure and composition

All the members in the MPX_3 family show a typical characteristic that $(P_2S_6)^{4-}$ or $(P_2Se_6)^{4-}$ anion sublattice is present within each layered crystal. While the metal ions are dispersed around the $(P_2X_6)^{4-}$ bipyramids in a honeycomb arrangement.[74] In Fig. 7b–d, we have shown the comparison of the crystal structure of the typical layered MoS_2 and MPX_3 systems. The van der Waals gap (the smallest gap between the S layers) in the MPX_3 system containing first-row transition metals is in the range of 3.22–3.24 Å, which is relatively higher than that of metal dichalcogenide (MS_2) systems.[74] Various metal cations can be accommodated in the MPX_3 system with a change in the size of the slab. As for the $(P_2X_6)^{4-}$ bipyramid structure modification,

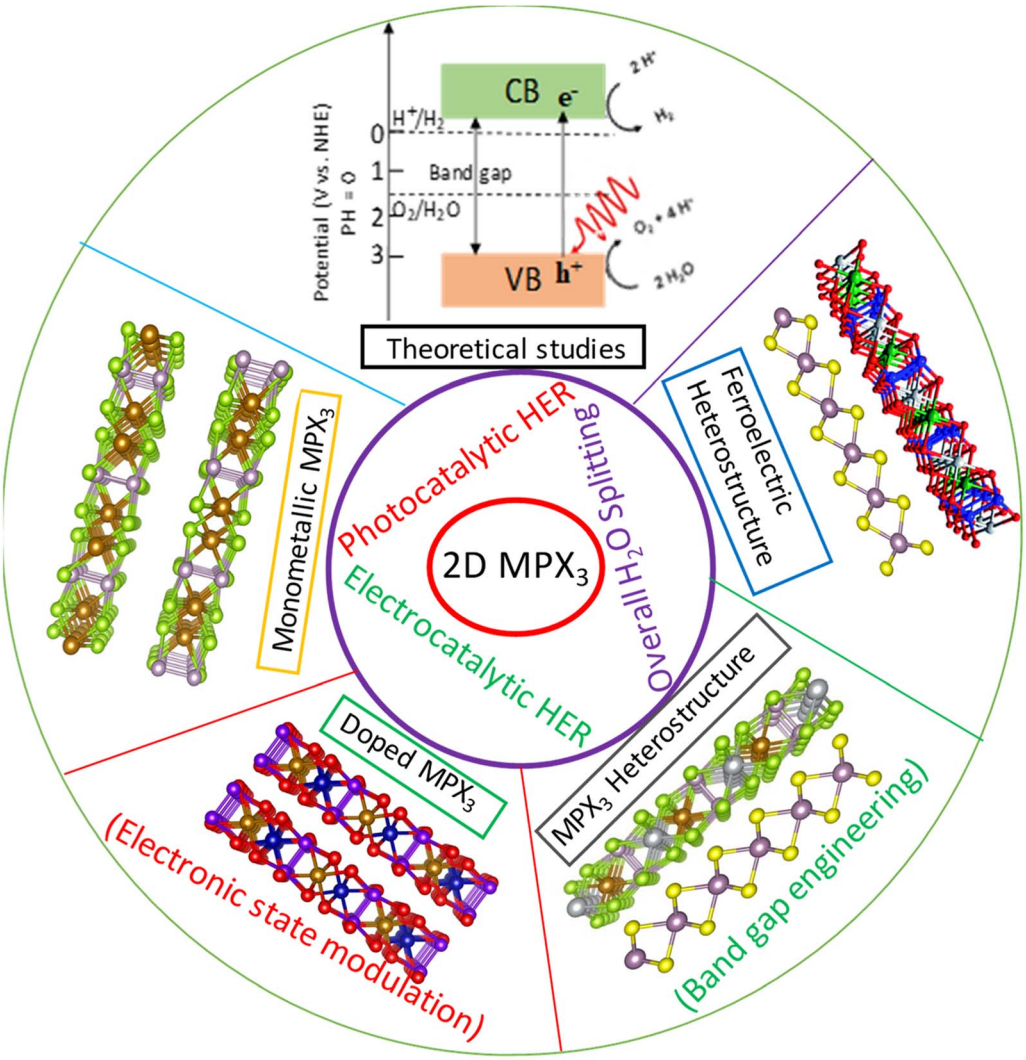

Fig. 6 Schematic highlights of 2D MPX_3 compounds and their nanocomposites for photocatalytic and electrocatalytic HER applications.

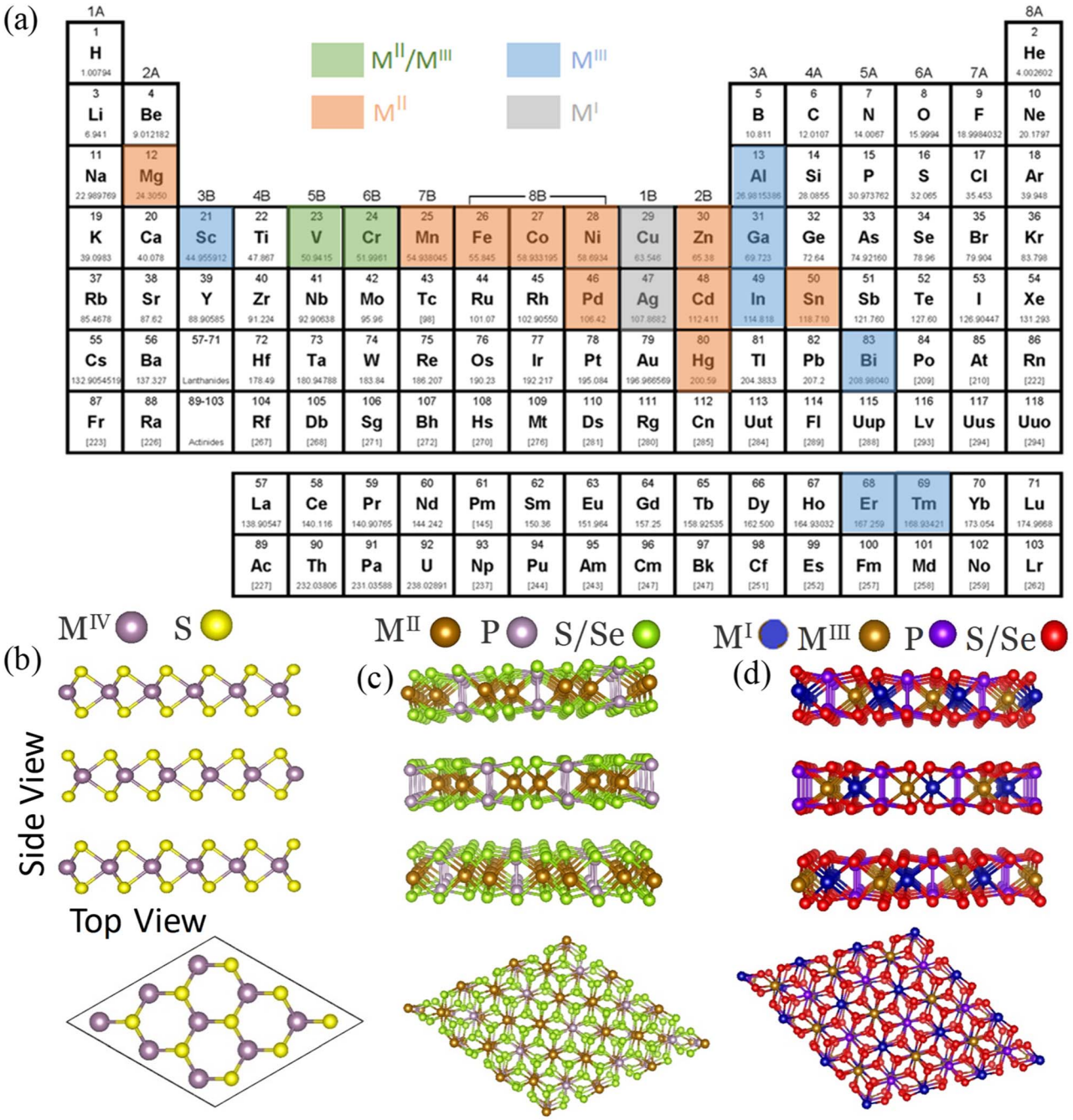

Fig. 7 Composition and crystal structure of MPX_3 compounds. (a) Periodic table highlighting the transition elements and their valence states constituting the MPX_3 system. Crystal structure of (b) MoS_2, (c) $M^{II}PQ_3$ (M^{II} = Zn, Cd, Mg; Q = S, Se) and (d) $Ag_{0.5}M^{III}{}_{0.5}PQ_3$ (M^{III} = Sc, In; Q = S, Se).

S^{2-} remains intact while the P–P bond distance is altered to accommodate metal ions of different sizes. An increase in P–P bond distance of 2.148 to 2.222 A^o is reported on substituting Cd^{2+} with Ni^{2+} in the MPS_3 system.[75] Besides, the layer thickness of the MPX_3 system is positively enhanced with an increase in P–P bond distance. On the cation side, the MPX_3 system can accommodate either divalent metal ions or a combination of monovalent and trivalent metal ions. In literature, bimetallic $Ni_2P_2S_{6-x}Se_x$,[76] $CuInP_2S_{6-x}Se_x$[77], and $Sn_2P_2S_{6-x}Se_x$[78] systems, with alloying of $(P_2S_6)^{4-}$ and $(P_2Se_6)^{4-}$ anion units are also reported. To date, MPX_3 systems containing Fe, Co, and Ni metal ions have been widely explored due to magnetic ordering and their catalytic properties towards photocatalytic and electrocatalytic water splitting.

2.1 Monometallic MPX_3

If there is only one type of metal occupying the cationic site of MPX_3, as shown in Fig. 7c, these systems are termed monometallic. It is convenient to study the $M^{II}PX_3$ system by comparing it with $M^{IV}S_2$ (example: MoS_2) crystal structure.

$M^{II}PX_3$ compounds can be visualized as a layered MS_2 system with 1/3 of the M site occupied by P–P (P_2) pairs, *i.e.*, $M^{II}_{2/3}(P)_{1/3}S_2$. The sulfur atom comprises surfaces within the individual lamella. The octahedrally coordinated $M^{II}PX_3$ system can be envisaged as M^{II} ions occupying the 2/3 site and the rest 1/3 site is filled by P–P pairs. Further, the P–P pair bonded to six sulfur atoms to form an ethane-like $(P_2S_6)^{2-}$ sublattice, within individual phosphor atoms tetrahedrally coordinated to three sulfur atoms. Meanwhile, the sulfur atom coordinated with two M^{II} ions and covalently attached to one phosphorous atom. Commonly, $M^{II}PS_3$ systems exhibit the *C*2/*m* symmetry with a monoclinic crystal structure and show a layer stacking sequence of "AAA".[79] The monoclinic lattice parameter β value calculated for $CoPS_3$ and $FePS_3$ is 107.16°, indicating that these systems possess an undistorted monoclinic crystal structure. On the other hand, $M^{II}PSe_3$ possess R3(−)H symmetry because of the higher P–Se bond distance and P–Se–P bond angle, whereas $NiPSe_3$ shows *C*2/*m* symmetry similar to $NiPS_3$.[80,81]

2.2 Bimetallic MPX_3

The "M" atom of MPX_3 can be exchanged with other metal atoms, containing home and hetero-charge substitutions. For instance, in systems such as $Zn_{1-x}Fe_xPS_3$, $Zn_{1-x}Ni_xPS_3$ (ref. 75) ($0 \leq x \leq 1$), and $Cd_xFe_{1-x}P_2S_6$ ($0 \leq x \leq 1$)[82] homo-charge distribution can be easily realized due to similar sizes of M_1^{II} and M_2^{II} ions. Most of the homo-charge mixed sulfides are monoclinic while selenides display trigonal symmetry. Hetero-chrage MPX_3 containing $\frac{1}{2}$ M_1^{I} (Ag or Cu) and $\frac{1}{2}$ M_2^{III} trivalent metal ion (Cr, V, Al or In) where "x" being S or Se atom are also reported. These mixed-cationic sulphides broadly show two stoichiometric ratios; $M^{1+}M^{3+}[P_2S_6]^{4-}$ (*e.g.*, $AgInP_2S_6$,[83] $AgScP_2S_6$ and $CuVP_2S_6$ (ref. 84)) and $M_2^{1+}M^{2+}[P_2S_6]^{4-}$ (*e.g.*, $Ag_2MgP_2S_6$ and $Ag_2MnP_2S_6$).[79] Among these sulfides, $AgInP_2S_6$, and $AgScP_2S_6$ are trigonal and centrosymmetric, while $CuVP_2S_6$ is non-centrosymmetric. Mixed selenides exist in two stoichiometry: $M^{1+}M^{3+}[P_2Se_6]^{4-}$ (*e.g.*, $CuAlP_2Se_6$ (ref. 85) with random Cu^{1+} and Al^{3+} arrangement) and $M_{4/3}{}^{3+}Y_{2/3}[P_2Se_6]^{4-}$, where Y signifies an unfilled site (*e.g.*, $In_{4/3}P_2Se_6$).[86]

3. Synthetic methods

Production of single-layer graphene from graphite by the scotch-tape method has opened a plethora of opportunities for researchers to realize other atomically-thin 2D materials such as MoS_2, phosphorene, and bismuthene.[87,88] Lee *et al.* successfully adapted micromechanical exfoliation of bulk $MnPS_3$ to prepare a few-layer $MnPS_3$ of high-quality and large lateral size.[89] Fig. 8a–c shows the optical microscopy and atomic force microscopy (AFM) images of the few-layer $MnPS_3$. Using the AFM height profile graph one can easily find out the number of stacked layers and lateral dimension of the nanosheet. For large-scale exfoliation, physical routes such as ball milling and liquid-phase exfoliation[90,91] in solvents such as N, *N*-dimethylformamide, and *N*-methyl-2-pyrrolidone have been reported. In addition, the chemical vapor deposition (CVD) strategy is also used to prepare monolayers of $MnPS_3$.[65] The CVD strategy involves simultaneous phosphorization and sulfurization of the MnO_2 template using sulfur and phosphor precursors, respectively in the two-zone furnace. $MnPSe_3$ has also been synthesized by the CVD method by utilizing a Se source instead of S powder. Recently, Li *et al.*[92] exfoliated bulk Ni_2PS_3 in an electrolyte containing tetra-*n*-butylammonium tetrafluoroborate as cationic intercalation salt by applying bias voltage (−3 V) to the bulk electrode and obtained exfoliated sheets in higher yields. The mechanism involves the intercalation of tetra-*n*-butylammonium salts, which considerably declines the van der Waals attractions between the stacked layers. Then, after applying voltage for a longer time, the intercalated tetra-*n*-butylammonium decomposes into the gaseous species which assists in delamination of the sheets from stratified bulk $NiPS_3$ crystals.

Rao and coworkers[93] extended the chemical vapor transport (CVT) method to prepare monometallic ($MnPS_3$, $FePS_3$, $NiPS_3$, $ZnPS_3$, $CdPS_3$, $FePSe_3$, and $CdPSe_3$) and bimetallic $Ag_{0.5}In_{0.5}PS_3$ and $Ag_{0.5}In_{0.5}PSe_3$) MPX_3 systems (Fig. 8d and e). The synthesis involved heating the stoichiometric ratios of the constituent elements sealed in a quartz ampoule to ∼700 °C under an inert atmosphere. The pure bulk MPX_3 compounds were formed at the other end of the quartz ampoule. The presence of sulfur and phosphor elements enhanced the vapor transport rate during material growth and well-developed crystals are obtained. The obtained bulk crystals were exfoliated in a water and ethanol mixture under sonication conditions. Fig. 8f and g shows the TEM images of the exfoliated $Ag_{0.5}In_{0.5}PS_3$ and $Ag_{0.5}In_{0.5}PSe_3$ systems, which revealed a few-layer nature. In literature, the majority of MPX_3 at large-scale are prepared using the CVT method and this strategy is even applicable for doping other transition (Ni, Fe or Co) elements into $MnPS_3$ (ref. 94) as well as for the synthesis of ferroelectric $CuInP_2S_6$ (ref. 95) and $CuBiP_2S_6$ materials.

4. Electrocatalysis

Electronic structure analysis can predict probable reasons behind the catalytic activity of various materials. Orbitals of both metal and non-metal impact the catalytic activity depending on the redox reaction and related interactions. Transition metals require $d_z{}^2$ orbitals for hydrogen adsorption, while oxygen evolution reactions require d_{xz} and d_{yz} orbital O^{2-}, OH^-, and OOH^- adsorption. The catalytic system involving all three orbitals (d_{xz}, $d_{yz,}$ and $d_z{}^2$) is considered to be superior for overall water splitting. In the case of a non-metallic system, P and S atoms are reported to be active sites for electrochemical reactions. The hydrogen adsorption free energy (Δ_{GH}) of a catalyst is broadly recognized as a good descriptor in evaluating the H_2 evolution activity of a particular material.[47] The ideal catalyst should possess a thermoneutral H^+ adsorption value. Song *et al.*[96] calculated the Δ_{GH} value on the basal plane and edges of $NiPS_3$, $FePS_3$, and $NiFePS_3$ compounds using DFT calculations (Fig. 9a). These calculations suggested that the Δ_{GH} value on the basal plane of $NiPS_3$, $FePS_3$, and $NiFePS_3$ is very high (∼0.5 eV). Interestingly, 10% Fe-doped $NiPS_3$ formed $Ni_{0.9}Fe_{0.1}PS_3$; the Δ_{GH} value on P and S edge sites was reduced to the

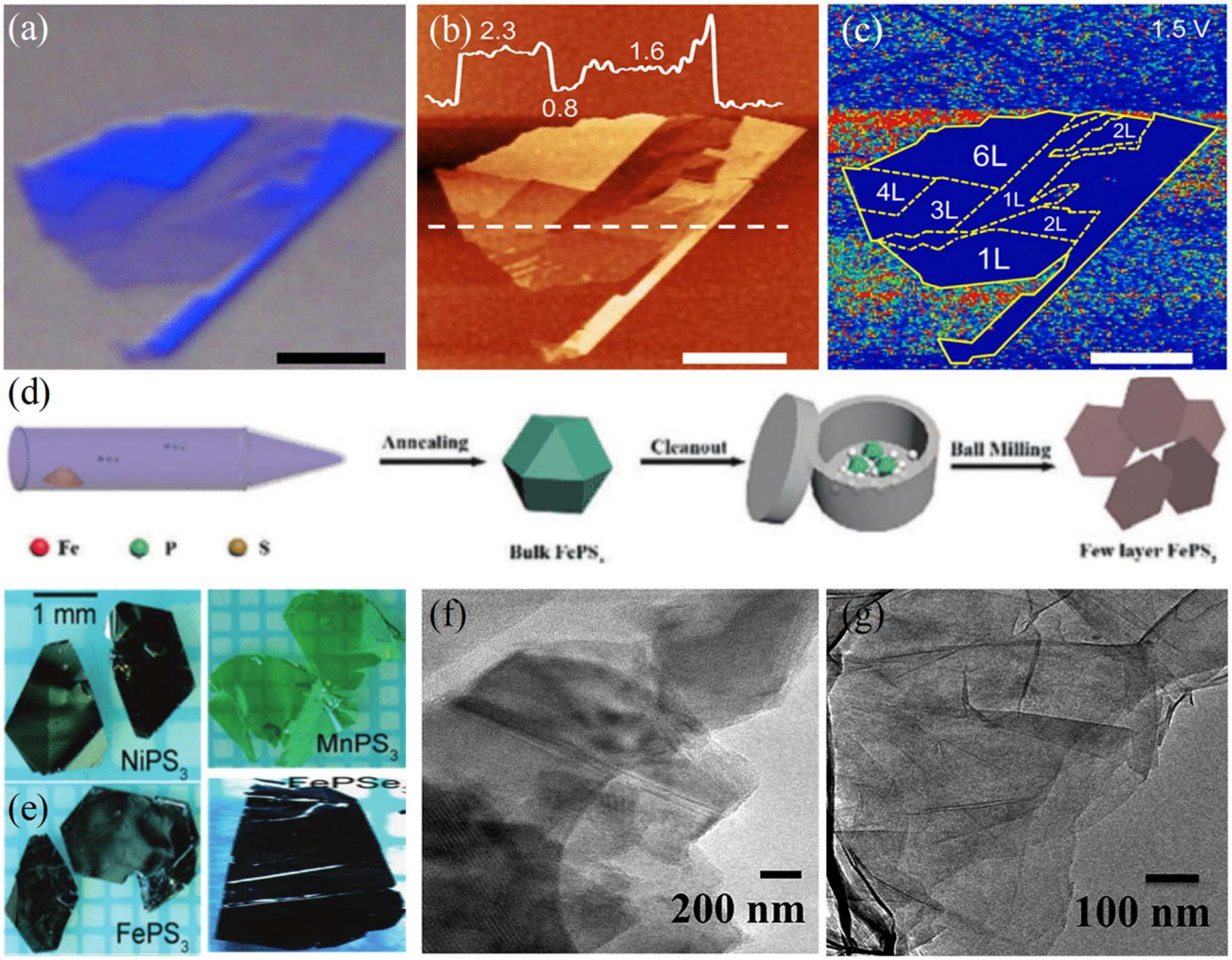

Fig. 8 (a) Optical microscopy, (b) AFM, and (c) conductive AFM image of few-layer $MnPS_3$ obtained by the scotch-tape exfoliation method. Adapted with permission.[89] Copyright 2016, AIP Publishing. (d) Schematic representation of the CVT method adapted for the preparation of MPX_3 crystals and (e) photographs of the bulk $NiPS_3$, $FePS_3$, $MnPS_3$, and $FePSe_3$ prepared by the CVT method. TEM images of the exfoliated (f) $Ag_{0.5}In_{0.5}PS_3$ and (g) $Ag_{0.5}In_{0.5}PSe_3$ nanosheets.[93]

thermoneutral value, indicating that the bimetallic MPX_3 systems can be an ideal catalyst for HER. In another study, Sun *et al.*[97] anchored different transition metals (*e.g.*, Sc, Ti, V, Cr, Mn, Fe, Co, and Ni) on monolayer $CuPS_3$ and examined the catalytic performance towards HER. As shown in Fig. 9b, V, Fe, and Ni decorated $CuPS_3$ were situated at the peak of the volcano curve, suggesting that these systems are potentially good for water splitting. Further, the authors also calculated the influence of hydrogen cover rate and found that V anchored $CuPS_3$ was catalytically active for HER over a wide hydrogen coverage. Apart from the Δ_{GH} value, the electron transport ability at active sites of the catalyst plays a crucial role in determining the overall HER activity. In view of this, Mayorga *et al.*[98] calculated the heterogeneous electron-transfer (HET) rates for $CrPS_4$, $MnPS_3$, $FePS_3$, $CoPS_3$, $NiPS_3$, $ZnPS_3$, $CdPS_3$, $GaPS_4$, $SnPS_3$, and $BiPS_4$ using cyclic voltammograms recorded in $[Fe(CN)_6]^{3/4}$ redox couple by the Nicholson's method (Fig. 9c). The HET performance of $BiPS_4$ (k^o_{obs} ~0.024 cm s^{-1}) was comparable with a glassy carbon substrate, which then decreased in the following order $CdPS_3$ > $CrPS_4$ > $SnPS_3$ > CoPS. The HET rate is generally related to the inherent orbital orientation of the particular material and higher HET in the case of $BiPS_4$ suggests that this catalyst is electrochemically more active than the other studied MPX_3 systems. Further, the charge-transfer resistance (R_{ct}) calculated for MPX_3 using electron impedance spectroscopy is in the range of 0.5 to 6.5 kΩ with $CdPS_3$ and $BiPS_4$ showing lower R_{ct} value, indicating that these MPX_3 systems are semiconducting in nature (Fig. 9d). Incorporation of conducting matrix such as graphene and carbon nanotubes is reported to enhance charge-transfer characteristics and HER yield of some MPX_3 systems.[47]

During electrolytic water splitting, the catalyst material is coated on the substrate (glassy carbon and indium tin oxide) and utilized as the anode. As depicted in Fig. 10a, the water-splitting electrolyzer consists of three main constituents, the anode, cathode, and electrolyte. Irrespective of the electrolytic

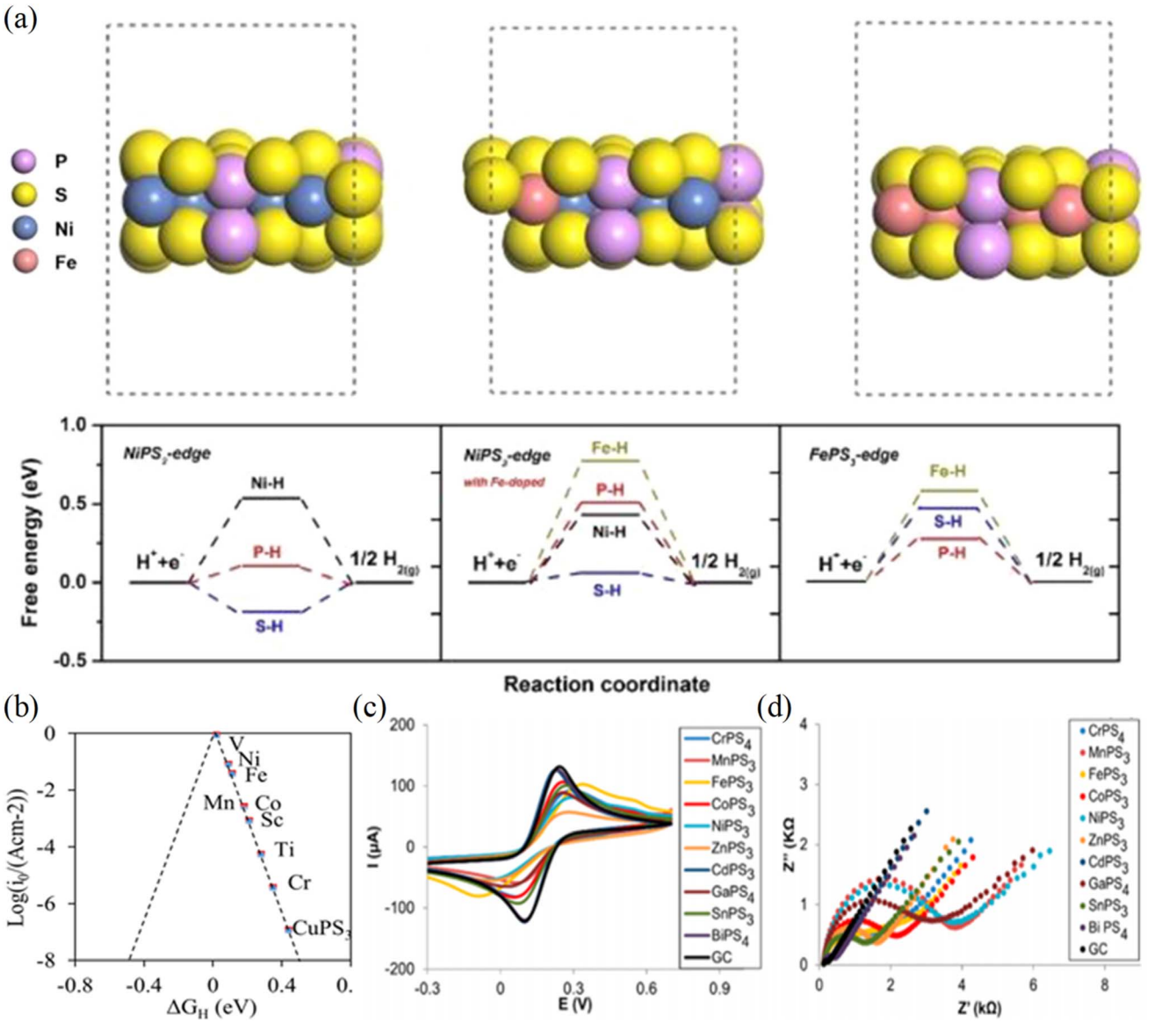

Fig. 9 (a) Structure and the corresponding free energy diagram of hydrogen evolution at equilibrium for $NiPS_3$, $Ni_{0.9}Fe_{0.1}PS_3$, and $FePS_3$. Reprinted with permission.[96] Copyright 2019, American Chemical Society. (b) The Volcano curve of exchange current density for various transition metal anchored $CuPS_3$. Reprinted with permission.[97] Copyright 2022, Springer. (c and d) Cyclic voltammograms recorded in the ferri/ferrocyanide redox probe and the Nyquist plots of various 2D TMPCs. Reprinted with permission.[98] Copyright 2017, American Chemical Society.

media (acidic or basic), the water splitting reaction involves a change in free energy of 237 kJ mol^{-1} at 1 atm and 25 °C, corresponding to a theoretical cell voltage of 1.23 V to initiate water splitting.[99] However, experimentally a voltage higher than 1.23 V is required due to mass, electrolyte, and transport resistances and also because of the sluggish kinetics of HER and OER reactions.[100] The overpotential can be reduced by coating the catalyst at the anode and cathode surfaces, which decreases the energy barrier. Water splitting *via* HER involves the reduction of a H^+ ion or H_2O, based on the pH of the electrolytic medium.[100,101]

$$2H^+ + 2e^- \rightarrow H_2 \text{ (acidic)}$$

$$2H_2O + 2e^- \rightarrow 2OH^- + H_2 \text{ (basic)}$$

Under acidic conditions, HER follows three possible reaction pathways, namely Volmer, Tafel, or Heyrovsky pathways. The Volmer step involves the reaction of electrons with H_3O^+ to yield catalytically adsorbed H^+ ion (H_{ad}) ($2H^+ + e^- \rightarrow H_{ads}$). Subsequently, H_2 evolution occurs either by following the Tafel ($2H_{ads} \rightarrow H_2$) or Heyrovsky ($H_{ads} + H^+ + e^- \rightarrow H_2$) pathway or both (Fig. 10b).[41–43] Irrespective of the paths by which H_2 evolution happens, H_{ad} is always associated with the water reduction reaction. The Tafel plots could help in obtaining the reaction kinetics and mechanistic pathways for any catalyst, which shows water splitting *via* HER. The slope corresponds to the log(current density) *versus* overpotential plot, in the cathodic

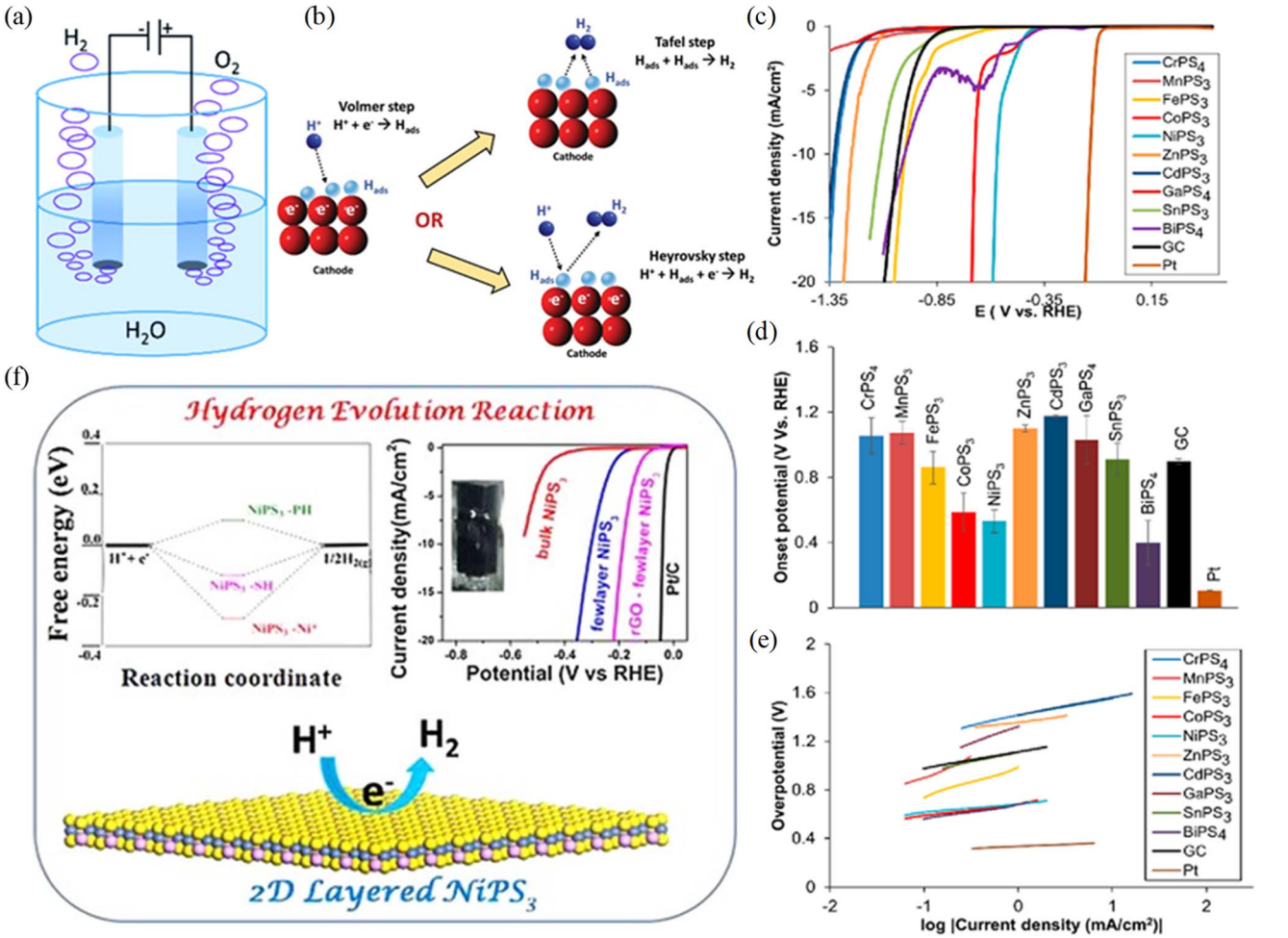

Fig. 10 Schematic of the (a) water-splitting electrolyzer and (b) possible reaction routes for electrocatalytic HER in the acidic medium. Reproduced with permission.[122] Copyright 2019, Elsevier. (c and d) Linear sweep voltammogram (LSV) curves obtained in 0.5 M H_2SO_4 and (e) Tafel plots for various bulk MPX_3. Reproduced with permission.[123] Copyright 2017, American Chemical Society. (f) Free energy diagram of the H_2 evolution for $NiPS_3$ and LSV curves of bulk $NiPS_3$, exfoliated $NiPS_3$, and $NiPS_3$/RGO composites. Reproduced with permission.[106] Copyright 2016, Wiley publication.

potential (η) range, which gives the Tafel slope value. The Tafel slope value signifies the amount of additional potential essential to increase a current density by 10 mA cm^{-2}. For an ideal catalyst Pt, the Tafel slope values of 30, 40, and 120 mV dec^{-1} indicate that the Volmer, Heyrovsky, and Tafel steps are the rate-determining steps.[102,103] The charge carrier mobility and the number of active sites also play an important role in describing the intrinsic HER activity for MPX_3. For instance, $MnPSe_3$ shows high charge carrier mobility (electron and hole mobilities of 625.9 and 34.7 $cm^2\ V^{-1}\ S^{-1}$, respectively), and the massive divergence in the carrier mobility values suggests that efficient charge-separation for H_2 and O_2 evolution reactions.[66] Further, exfoliated layers show high water redox activity compared to the bulk due to increasing in-plane conductivity and more exposed edge sites.

2D MPX_3-based electrocatalysts display H_2 evolution activity starting from very low to high, some of them even showing activity comparable to benchmark Pt/C catalysts. Experimentally, the electrocatalytic HER performance is accessed by the onset potential with respect to a standard hydrogen electrode, Tafel slope, and charge-transfer resistance concerning the benchmark Pt/C catalyst. The lower the value of these factors, the superior the catalytic activity. We have compared these parameters of 2D MPX_3-based catalysts in Table 1, which suggest that the MPX_3 containing Ni, Co, and Fe atoms, bimetallic TMPCs and their composite with other 2D systems display superior activity. Generally, it has been described that bimetallic phosphochalcogenides show better activity than monometallic systems due to synergistic interactions. Some of the widely examined 2D MPX_3 and their heterostructures are discussed in the following section.

In recent work, Martinez *et al.*[98] studied the electrocatalytic HER performance of a series of bulk MPX_3 (M = Mn, Fe, Co, Ni, Zn, Cd, Ga, and Sn) in acid electrolytes. Fig. 10c and d show the HER polarization curves for these MPS_3 compounds and the resulting onset potential values at 10 mA cm^{-2}. Among these MPX_3 compounds, only $NiPS_3$ and $CoPS_3$ showed lower overpotential, −590 and −530 mV (*vs.* RHE), respectively, than bare

Table 1 Comparison of electrocatalytic HER activity of 2D TMPCs and their nanocomposites reported in the literature

Catalysts	Electrode substrate	Overpotential at 10 mA cm^{-2} *vs.* RHE (mV)	Tafel slope (mV dec^{-1})	Electrolyte	Reference
Exfoliated MPX_3 nanosheets					
$MnPS_3$	GCE[a]	835 ± 68	—	0.5 M H_2SO_4	124
$MnPS_3$	GCE	632	272	0.5 M H_2SO_4	94
$MnPS_3$	GCE	1090 ± 71	—	0.1 M KOH	124
$MnPSe_3$	GCE	640 ± 87	—	0.5 M H_2SO_4	124
$MnPSe_3$	GCE	992 ± 56	—	0.1 M KOH	124
$FePS_3$	GCE	211 ± 3	42	0.5 M H_2SO_4	47
$FePS_3$	GCE	337 ± 4	—	1M KOH	47
$FePS_3$	GCE	673 ± 4		3.5 wt% NaCl	47
$FePS_3$	GCE	530	56	0.5 M H_2SO_4	98
$CoPS_3$	Graphite	222 ± 2	71 ± 5	0.5 M H_2SO_4	125
$CoPS_3$	GCE	590	84	0.5 M H_2SO_4	98
$NiPS_3$	GCE	297	69	0.5 M H_2SO_4	106
$NiPS_3$	GCE	398	159	1M KOH	106
$NiPS_3$	GCE	816	54	3.5 wt% NaCl	106
$NiPS_3$	GCE	205	74	0.5 M H_2SO_4	126
MPX_3 nanosheet composite with reduced graphene oxide (RGO)					
$FePS_3$/RGO	GCE	108 ± 2	54	0.5 M H_2SO_4	47
$FePS_3$/RGO	GCE	467 ± 3	—	1M KOH	47
$FePS_3$/RGO	GCE	192 ± 2	—	3.5 wt% NaCl	47
$NiPS_3$/RGO	GCE	178	55	0.5 M H_2SO_4	106
$NiPS_3$/RGO	GCE	281	48	1M KOH	106
$NiPS_3$/RGO	GCE	543	94	3.5 wt% NaCl	106
Transition element doped MPX_3 nanosheets					
$Ni_{0.9}5Fe_{0.05}PS_3$	GCE	130	114	1M KOH	96
$Ni_{0.9}Fe_{0.1}PS_3$	GCE	72	73	1M KOH	96
$Ni_{0.85}Fe_{0.15}PS_3$	GCE	152	187	1M KOH	96
$Ni_{0.95}Mn_{0.05}PS_3$	GCE	—	135	1M KOH	94
$Ni_{0.90}Mn_{0.10}PS_3$	GCE	—	142	1M KOH	94
$Ni_{0.85}Mn_{0.15}PS_3$	GCE	—	143	1M KOH	94
$Ni_{0.97}Co_{0.03}PS_3$	GCE	112	103	1M KOH	49
$Ni_{0.95}Co_{0.05}PS_3$	GCE	71	77	1M KOH	49
$Ni_{0.93}Co_{0.07}PS_3$	GCE	105	110	1M KOH	49
$Ni_{0.91}Co_{0.09}PS_3$	GCE	145	113	1M KOH	49
$Co_{0.6}(VMnNiZn)_{0.4}PS_3$	GCE	66	65	1M KOH	107
$MnFePS_3$	Carbon paper	102	49	1M KOH	127
$NiCoFePS_3$	Ni foam	231	86	1M KOH	128
Single-atom anchored MPX_3 nanosheets					
$NiFePS_3$	GCE	356	170	1M KOH	109
$CoFePS_3$	GCE	490	132	1M KOH	109
$PdFePS_3$	GCE	471	128	1M KOH	109
2D MPX_3–based heterostructures					
$FePS_3/MoS_2$	Ni foam	175	127	0.5 M H_2SO_4	50
$FePS_3/MoS_2$	Ni foam	168	107	1 M KOH	50
$NiPS_3/MoS_2$	GCE	112	64	1 M KOH	51
$NiPS_3/Ni_2P$	GCE	85	82	1 M KOH	110
$NiPS_3$/Ni foam	Ni foam	74	86	1 M KOH	129
$CoNiPS_3$/N-doped carbon	GCE	140	60	1 M KOH	130

[a] GCE – glassy carbon electrode.

GCE (−890 mV *vs.* RHE), indicating that these systems can be beneficial for electrocatalysis.[69,98] The high H_2 evolution activity of $NiPS_3$ and $COPS_3$ is ascribed to preferential orientation of these systems in the (001) crystal plane, as these planes are reported to be highly HER active in the case of Ni_2P catalyst.[33,104] Further, the MPS_3 system containing Ni and Co metals is estimated to display ΔG_{H^*} value near to thermoneutral potential, thereby display superior HER activity.[49,92,105] In another study, Sampath and coworkers[106] have shown that HER activity of bulk $NiPS_3$ can be further improved by exfoliating bulk crystals into few-layers by liquid phase exfoliation. These few-layer $NiPS_3$ showed stable H_2 evolution over a long period in

a wide pH range of 1 to 14, including in 3.5 wt% NaCl solution, which is close to seawater composition. Fig. 10f shows the *iR*-corrected LSV polarization curves for bulk and exfoliated $NiPS_3$, which show the onset potential of −450 and −159 mV, respectively, in 0.5 M H_2SO_4, indicating a higher activity in the case of the latter. Further, bulk $NiPS_3$ exhibited a Tafel slope value of −119 mV dec^{-1}, while a few-layer sample revealed a value of −69 mV dec^{-1}. Further, exfoliated $NiPS_3$ showed an overpotential of 297, 398 and −816 mV in acidic (pH = 1), basic (pH = 14) and in neutral 3.5 wt% NaCl electrolyte, respectively, at 10 mA cm^{-2}. These studies indicate that the kinetics of HER is more facile in the case of exfoliated samples due to an enhanced charge-transfer rate. The authors also showed by DFT calculation that the P atom is the most favorable site for hydrogen adsorption by evaluating the ΔG_{H^*} value (Fig. 10f).

Sampath and coworkers[47] reported HER activity of the exfoliated $FePS_3$ system as well. The reported overpotentials at 10 mA cm^{-2} for exfoliated $FePS_3$ in pH = 1, 14, and in neutral 3.5 wt% NaCl were −211, −337, and −637 mV respectively. According to Sampath and coworkers, exfoliated $NiPS_3$ showed higher overpotential at 10 mA cm^{-2} and hence lower activity than $FePS_3$. On the contrary, Martinez *et al.*[98] reported that bulk $NiPS_3$ showed lower overpotential at 10 mA m^{-2} as compared to $FePS_3$. Therefore, the physicochemical properties of these materials need to be investigated in detail to provide further insights into the activity and mechanism of H_2 evolution. In addition, coupling of exfoliated $NiPS_3$/$FePS_3$ with conductive reduced graphene oxide (RGO) substrate further improved HER activity as reported by Sampath and coworkers.[47,106] The onset potential values obtained for exfoliated $NiPS_3$ and $FePS_3$ were −159 mV and −95 mV, while $NiPS_3$/RGO and $FePS_3$/RGO show −62 and −50 mV, respectively. The charge-transfer resistance (R_{ct}) value obtained from AC impedance measurements indicates that the R_{ct} value for $NiPS_3$ and $FePS_3$ was lowered on coupling with graphene. This implied that the conductive RGO support improved the HER activity of the MPX_3 system due to enhanced charge-transfer characteristics. Also, $NiPS_3$/RGO and $FePS_3$/RGO nanocomposites showed long-term stability, suggesting these materials can be highly efficient electrocatalysts for HER in a wide pH range.

As indicated earlier, 2D MPS_3 showed marginal electrocatalytic performance due to poor electronic conductivity; thus conductive graphene is coupled to improve the HER performance. Even though, $NiPS_3$/RGO and $FePS_3$/RGO composite required overpotentials of −178 and −192 mV, respectively, to reach 10 mA cm^{-2} in a basic electrolyte. In general, the catalyst electrocatalytic activity can be improved either by increasing the active site through catalyst loading or exposing the edge site *via* nanostructuring, or enhancing the intrinsic activity of the individual site. With this in mind, Li *et al.*[49] doped Co into $NiPS_3$ and with $Ni_{0.95}Co_{0.05}PS_3$ nanosheets achieved a current density of 10 mA cm^{-2} at an overpotential of as low as −48 mV (*vs.* RHE) with a Tafe slope of 77 mV dec^{-1} in 1.0 M KOH electrolyte (Fig. 11a). The synthetic procedure involved initially obtaining the bulk $NiCoPS_3$ by heating the stoichiometric ratio of individual elements in a sealed quartz ampoule. Later, the bulk sample was ultrasonicated in *N*,*N*-dimethyl formamide solvent to obtain 2D nanosheets. The authors also prepared $Ni_{1-x}Co_x$-PS_3 containing various cobalt amounts ($x = 0.03$, 0.05, and 0.07) to know the effect of Co doping content on HER activity. The R_{ct} values of 18.6, 12.1, 23.4, and 41.7 Ω were obtained for Ni_{1-x}-Co_xPS_3 with cobalt doping amounts of $x = 0.03$, 0.05, 0.07, respectively, while bare $NiPS_3$ showed 82.3 Ω (Fig. 11b). The reduced R_{ct} value in the case of $Ni_{1-x}Co_xPS_3$ implied that Co doping improved intrinsic HER kinetics of $NiPS_3$ through a higher charge-transfer rate. However, an increase or decrease of Co amount other than $x = 0.05$, more or fewer declines HER performance. Later, theoretical studies have shown that H affinity at the P site can be improved by Co doping along with electrical conductivity.[48] In another study, Rakov *et al.*[94] showed that Ni-doped (lower oxophilicity) $MnPS_3$ displayed higher HER activity than the bare sample. With Ni doping, the ability of binding of the surface intermediate into the catalyst surface decreased, which in turn assisted the desorption steps such as the Tafel or Heyrovsky steps. In addition, doping of multi-metal atoms such as V, Mn, Ni, and Zn into $CoPS_3$ increased the density of active sites due to the formation of high entropy alloys.[107] The generated S edge sites and basal plane P sites improved H^+ ion adsorption, whereas Mn ion boosted water dissociation during the Heyrovsky step. Recently, Megha *et al.*[108] using DFT calculations showed that Sc, Y, and Mo elemental doping into the $MnPSe_3$ lattice reduced the Δ_{GH} value of pristine $MnPSe_3$ to 1.41 eV, to 0.24, 0.18, and 0.23 eV, respectively. Further, the density of state (DOS) plots suggested that DOS at the Fermi energy was infinite for 25, 12.5, and 6.25% Sc elemental doping concentrations in $MnPSe_3$, indicating activation of the inert basal plane of $MnPSe_3$ towards HER (Fig. 11c and d). Apart from metal atom doping, non-metal carbon doping can transform semiconducting $FePS_3$ into metallic form and show enhanced HER activity. The dopant with fewer electrons than the substitutional atom can improve electronic conductivity and also greatly activate surface sites for hydrogen adsorption. Further, C, N-codoping in $FePS_3$ pushed ΔG_H (−0.188 eV) value closer to zero and showed HER activity comparable to that of Pt/C with a small overpotential of 53.2 mV to achieve a current density of 10 mA cm^{-2}.[105] However, studies on non-metal doping in 2D MPX_3 are very limited and these systems need to be investigated in detail both by computational and experimental studies.

Recently, Tang *et al.*[109] showed that anchoring of single-atom (SA) catalysts such as Ni, Co, and Pd over 2D $FePS_3$ can tune the surface electronic structure and reinforces water adsorption and dissociation capacity for both OER and HER. DFT calculations showed that Ni SA anchored $FePS_3$ facilitated electron aggregation from Fe to Ni–S and enhanced electron-transfer rate at Ni and S sites (Fig. 11e and f). In addition, the electron-rich Ni site acted as an active site to diminish hybridization between O and Ni in Ni–$FePS_3$, thereby, facilitating conversion from O* to OOH* group and reducing the barrier for OER. Ni–$FePS_3$ delivered an outstanding performance as a bifunctional catalyst for water splitting with an overpotential of 356 and 287 mV at a current density of 10 mA cm^{-2} for HER and OER, respectively (Fig. 11g–i). This study indicates that engineering surface active sites at the atomic scale are an

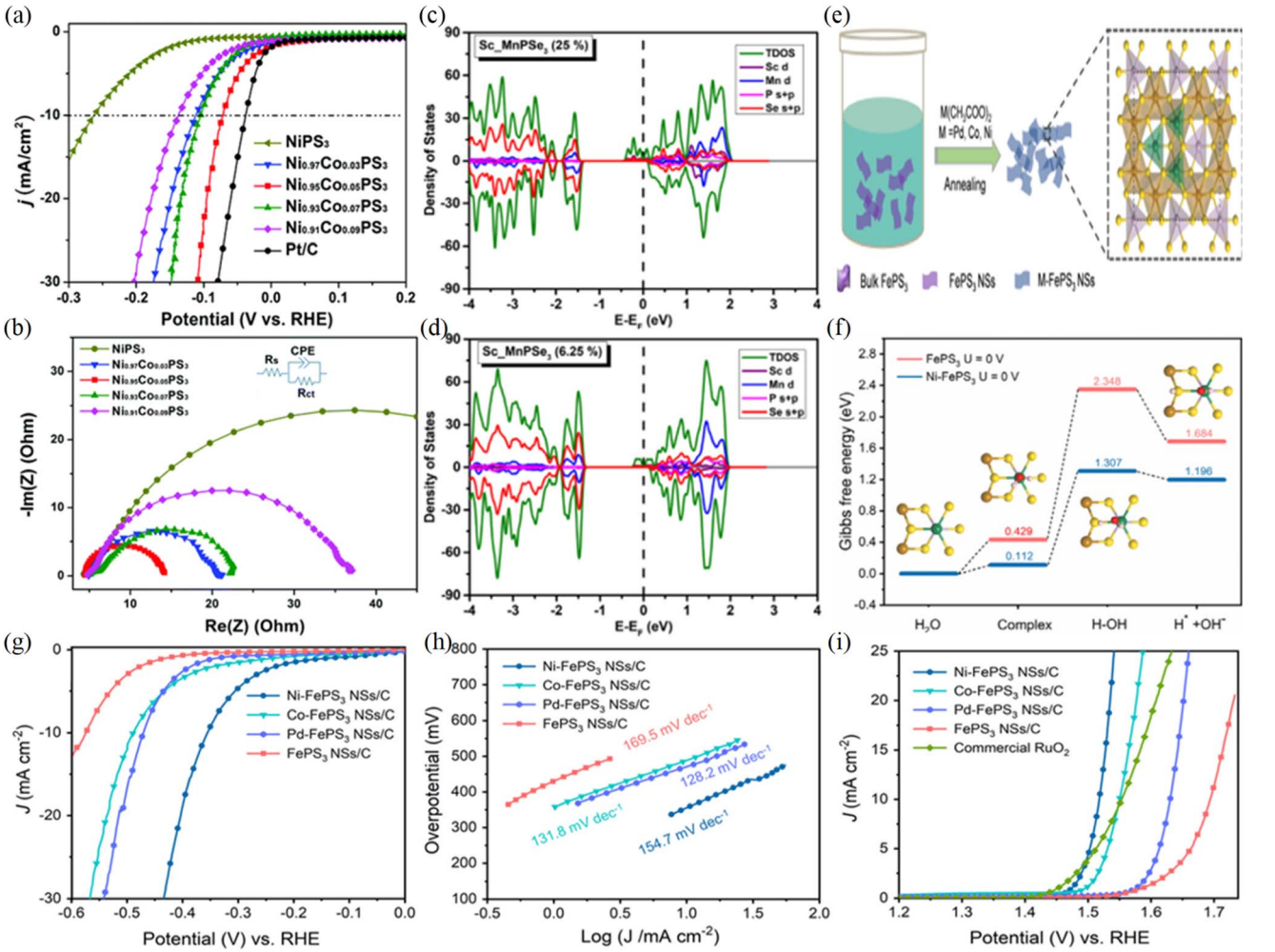

Fig. 11 (a) LSV polarization curves and (b) Nyquist plots for $Ni_{1-x}Co_xPS_3$ containing various cobalt amounts (x = 0.03, 0.05, 0.07).[49] (c and d) Density of states plots for 25 and 6.25% Sc element doped $MnPSe_3$. Reproduced with permission.[108] Copyright 2023, Elsevier. (e) Schematic illustration of anchoring single-atom catalysts (Pt, Co, and Ni) over 2D $FePS_3$. (f) Gibbs free energy profile of $FePS_3$ and Ni–$FePS_3$. (g and h) LSV polarization curves for HER and the corresponding Tafel plots, (i) polarization curves for OER for $FePS_3$, Ni–$FePS_3$, Co–$FePS_3$, and Pd–$FePS_3$ catalysts. Reproduced with permission.[109] Copyright 2022, Wiley publication.

effective way to modulate the catalytic activity of 2D MPX_3 systems.

MPX_3 nanostructures with a large number of active phosphorus edges are considered to be efficient water-splitting catalysts by both theoretical and experimental studies. The generation of heterojunctions by coupling two or more different materials can incorporate the advantages of distinct materials into one hybrid. Huang *et al.*[50] reported the 2D/2D $FePS_3/MoS_2$ heterojunction, in which interfacial coupling between $FePS_3$ and MoS_2 causes significant enhancement in H_2 evolution performance. $FePS_3/MoS_2$ requires low overpotentials of only 175 and 168 mV to reach 10 mA cm^{-2} current density under acidic and basic conditions, respectively (Fig. 12a and b). Further, $FePS_3/MoS_2$ showed lower Tafel slope values of 107 and 125 mV dec^{-1} at pH = 1 and pH = 14, respectively, with little decay in potential even after 1000 cycles (Fig. 12c). The *in situ* grown MoS_2 can provide more exposed active sites, which facilitate diffusion of active species and release of the formed H_2 bubble. Secondly, the intercalated MoS_2 layers can stop restacking of $FePS_3$ layers, enhancing conductivity and exposing active sites of $FePS_3$. Since the electron transfer resistance is higher in adjacent layers than along the MPX_3 layer, reduction in the stacking of the number of $FePS_3$ layers improves electronic conductivity and carrier flow to MoS_2.[50] In another study, Liu *et al.*[51] synthesized $NiPS_3/MoS_2$ composite and demonstrated that internal polarization field (IPF) facilities hydrogen spillover (HSo) during HER from the MoS_2 edge site to $NiPS_3$. Secondly, IPF boosts the hydroxyl ion diffusion pathway, thereby enhancing the rate of oxygen evolution reaction (Fig. 12d). The $NiPS_3/MoS_2$ composite requires a low overpotential of 112 and 296 mV to reach 10 mA cm^{-2} current density for H_2 and O_2 evolution reactions, respectively. Further, the $NiPS_3/MoS_2$ composite delivered overall water splitting with a cell voltage of 1.64 V at 10 mA cm^{-2} and exhibited long-term stability up to 100 h (Fig. 12e). The chronopotentiometry study conducted for 50 h indicates that $NiPS_3/MoS_2$ does not lose any

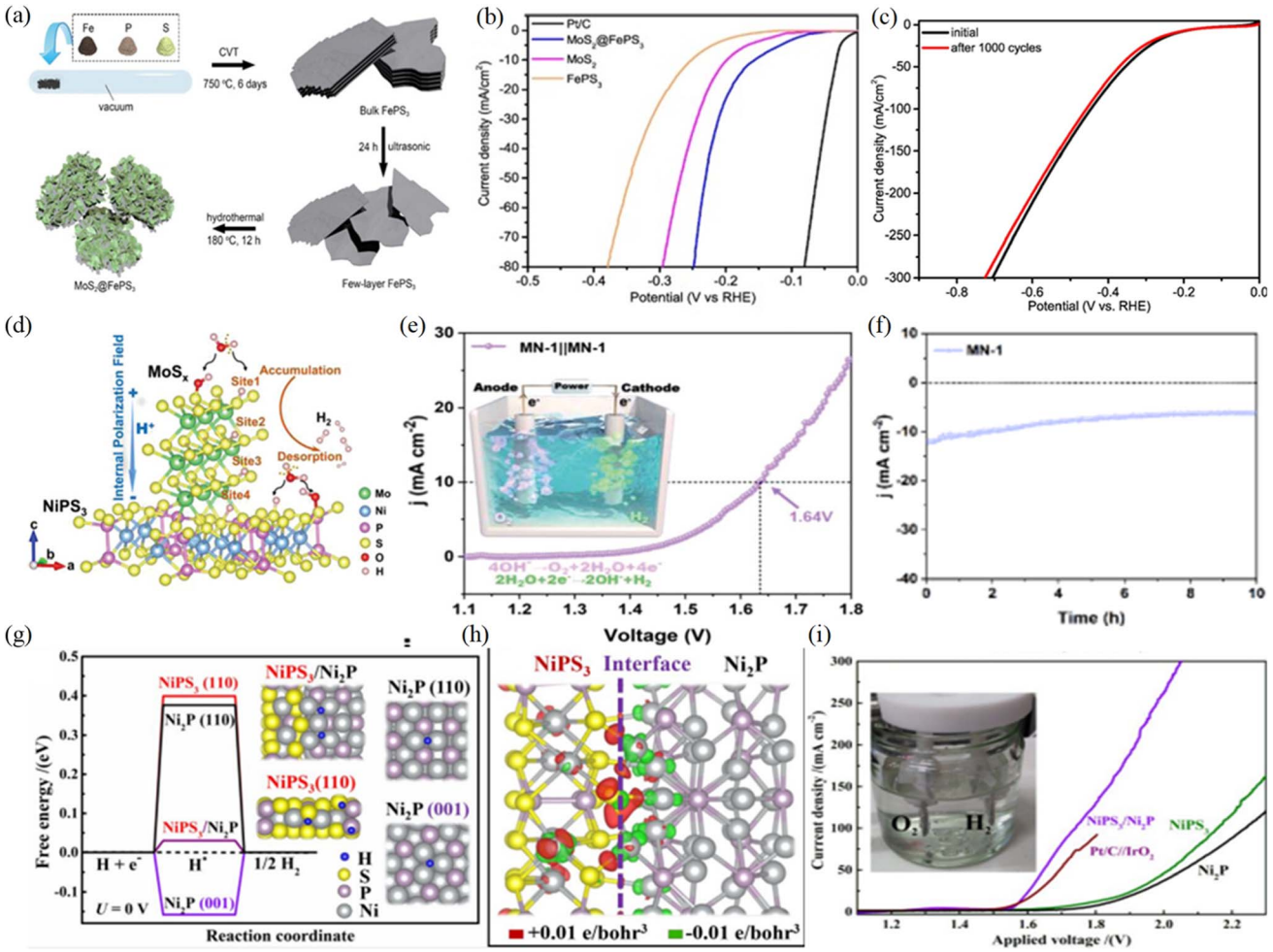

Fig. 12 (a) Schematic of the *in situ* CVT method adapted for the growth of $FePS_3/MoS_2$ heterostructure. (b) Polarization curves for $FePS_3/MoS_2$ heterostructure. (c) Electrochemical durability of $FePS_3/MoS_2$ in 0.5 M H_2SO_4. Reproduced with permission.[50] Copyright 2020, Elsevier. (d and e) Polarization curve of $NiPS_3/MoS_2$ as both anode and cathode catalyst for overall water splitting driven by a solar cell (~1.65 V). (f) Chronopotentiometry study for $NiPS_3/MoS_2$ carried for 50 h. Reproduced with permission.[51] Copyright 2012, Wiley publication. (g) Gibbs free energy of hydrogen adsorption estimated for $NiPS_3/Ni_2P$ composite, $NiPS_3$ (110), Ni_2P (110) and Ni_2P (110) planes. (h) Charge density distribution at the junction of $NiPS_3/Ni_2P$ composite. (i) Polarization curve of the $NiPS_3/Ni_2P$ heterocatalyst for overall water splitting compared with the benchmark $Pt/C//IrO_2$ electrocatalyst. Reproduced with permission.[110] Copyright 2019, American Chemical Society.

catalytic activity, implying the practical advantages of the catalyst in terms of stability (Fig. 12f). Besides, Liang *et al.*[110] grew nickel phosphide nanostructures on $NiPS_3$, which showed a lower bias voltage of 1.65 V for overall water splitting, even surpassing that of the commercial $Pt/C//IrO_2$ electrocatalyst (Fig. 12g–i). Generation of the MPX_3 heterostructure with MoS_2 would be beneficial as a bifunctional catalyst since these systems decrease the energy barrier for hydrogen adsorption and also improve sluggish OER kinetics due to built-in electric field gradient.[115]

5. Photocatalytic water splitting

2D MPX_3 compounds band gap ranges from 1.3 to 3.5 eV, which appears to be advantageous for optoelectronic and catalysis applications. Secondly, abundant active sites such as P and S edges of 2D MPX_3 facilitate hydrogen adsorption and desorption, these characteristics extend their application as photocatalysts for water-splitting applications. In this context, Shifa *et al.*[65] prepared $MnPS_3$ and $MnPSe_3$ nanosheets by the CVD method and examined their photocatalytic HER performance under solar light (AM 1.5G) without any sacrificial agent. Atomic force microscopy images revealed that $MnPS_3$ and $MnPSe_3$ show layer thicknesses of ~6 and 28 nm with lateral dimensions of ~1.5 and 0.45 μm, respectively (Fig. 13a and b). Tauc plots derived from UV-vis diffuse reflectance spectroscopy show a red shift in absorption edge for the $MnPSe_3$ as compared to $MnPS_3$, indicating the better light harvesting capability of the former system (Fig. 13c). As depicted in Fig. 13d, both $MnPS_3$ and $MnPSe_3$ showed good HER activity with H_2 evolution rates of 3.1 and 6.5 μmol h^{-1} g^{-1}, respectively. The high H_2 evolution rate of $MnPSe_3$ as compared to $MnPS_3$ can be ascribed to the superior light-harvesting ability and high charge carrier mobility in the former system. Secondly, the higher

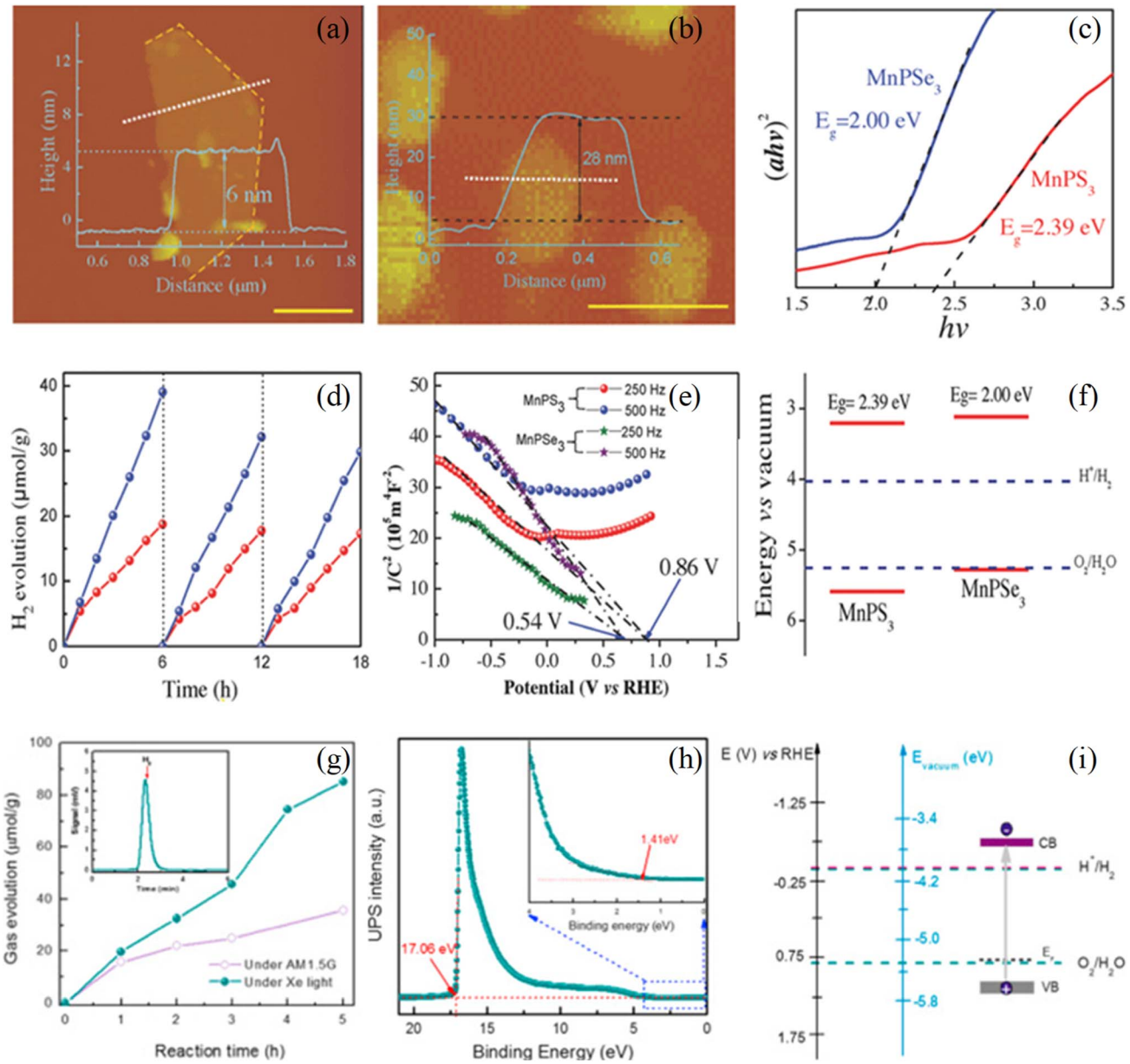

Fig. 13 AFM images of $MnPS_3$ (a), $MnPSe_3$ (b), Tauc plot (c), HER data (d), Mott–Schottky plots (e), and schematic illustration of alignment of VBM and CBM edge potentials with respect to water reduction potential derived from Mott–Schottky plots (f) for $MnPS_3$ and $MnPSe_3$. Reprinted with permission.[65] Copyright 2018, Wiley publication. Two-dimensional $NiPS_3$ HER data under a xenon lamp and in solar simulated light (g), ultraviolet photoelectron spectroscopy data (h), and schematic illustration of alignment of VBM and CBM edge potentials of $NiPS_3$ with respect to water reduction potential derived from Mott–Schottky plots (i). Reproduced with permission. Copyright 2017, Elsevier.[113]

electronegativity of Se compared to S of $P_2X_6^{4-}$ cluster orbitals could result in better H^+ adsorption and H_2 desorption. Further, the addition of Na_2S/Na_2SO_3 as a sacrificial electron donor enhanced the H_2 evolution rate of the $MnPS_3$ and $MnPSe_3$ photocatalysts to 21.2 and 43.5 μmol h^{-1} g^{-1}, respectively. The energy level of $MnPSe_3$ as derived from the Mott–Schottky plots indicated that VB was just fractionally below the water oxidation potential, which defied the oxygen evolution characteristics (Fig. 13e and f). Even though $MnPSe_3$ showed promising HER performance, most of the research on the $MnPSe_3$ system still focused on studying fundamental physical characteristics.

Layered metal thiophosphates containing Fe, Ni, Sn, and Zn have also been reported as efficient catalysts for photocatalytic hydrogen evolution reactions. For instance, Sendeku *et al.*[111] synthesized $Sn_2P_2S_6$ nanosheets with Pc monoclinic phase by chemical vapor conversion process employing SnS_2, P, and S precursors (Fig. 14a and b) and further utilized for H_2 generation from pure water under solar light irradiation. To reveal the light-harvesting ability of Sn_2P2S_6, the UV-vis diffuse reflectance spectrum was recorded, as shown in Fig. 14c. The absorption edge of $Sn_2P_2S_6$ was up to 520 nm with a weak absorption in the 520–600 nm region. Meanwhile, the corresponding Tauc plot

shown in the inset of Fig. 14c shows the estimated band gap (E_g) value of 2.25 eV. Further, Mott–Schottky plots gave a positive slope revealing the n-type feature along with a flat band potential of −0.48 V (Fig. 14d). Secondly, ultraviolet photoelectron spectroscopy (UPS) studies were also carried out to obtain the band alignment of $Sn_2P_2S_6$ nanosheets. From the UPS spectrum, the VB edge of $Sn_2P_2S_6$ was calculated to be at −5.68 *versus* the vacuum level, as shown in Fig. 14e. The CB level was calculated from the equation $E_{CB} = E_{VB} - E_g$, which was estimated to be at −3.43 eV *versus* the vacuum level. On the basis of the previous results, a schematic band diagram of $Sn_2P_2S_6$ is described in Fig. 14e, which implied that the VB and CB edges were suitably oriented to employ a water redox reaction. Fig. 14f shows the time course hydrogen evolution curve of $Sn_2P_2S_6$ under simulated solar light (AM 1.5G) without any sacrificial agent. The H_2 evolution rate increases linearly over time with a rate of 202.06 μmol h^{-1} g^{-1}, which is ~10 times higher than previously discussed $MnPS_3$ nanosheets. In another study, Zhao *et al.*[112] prepared exfoliated $ZnPS_3$ by a liquid-phase exfoliation from its bulk crystal and realized a high HER activity of 640 μmol h^{-1} g^{-1} under a xenon lamp using Na_2S and Na_2SO_3 as sacrificial agents (Fig. 14g–i). While bulk $ZnPS_3$ showed relatively low activity of 640 μmol h^{-1} g^{-1} under similar conditions. The enhanced activity in the case of exfoliated

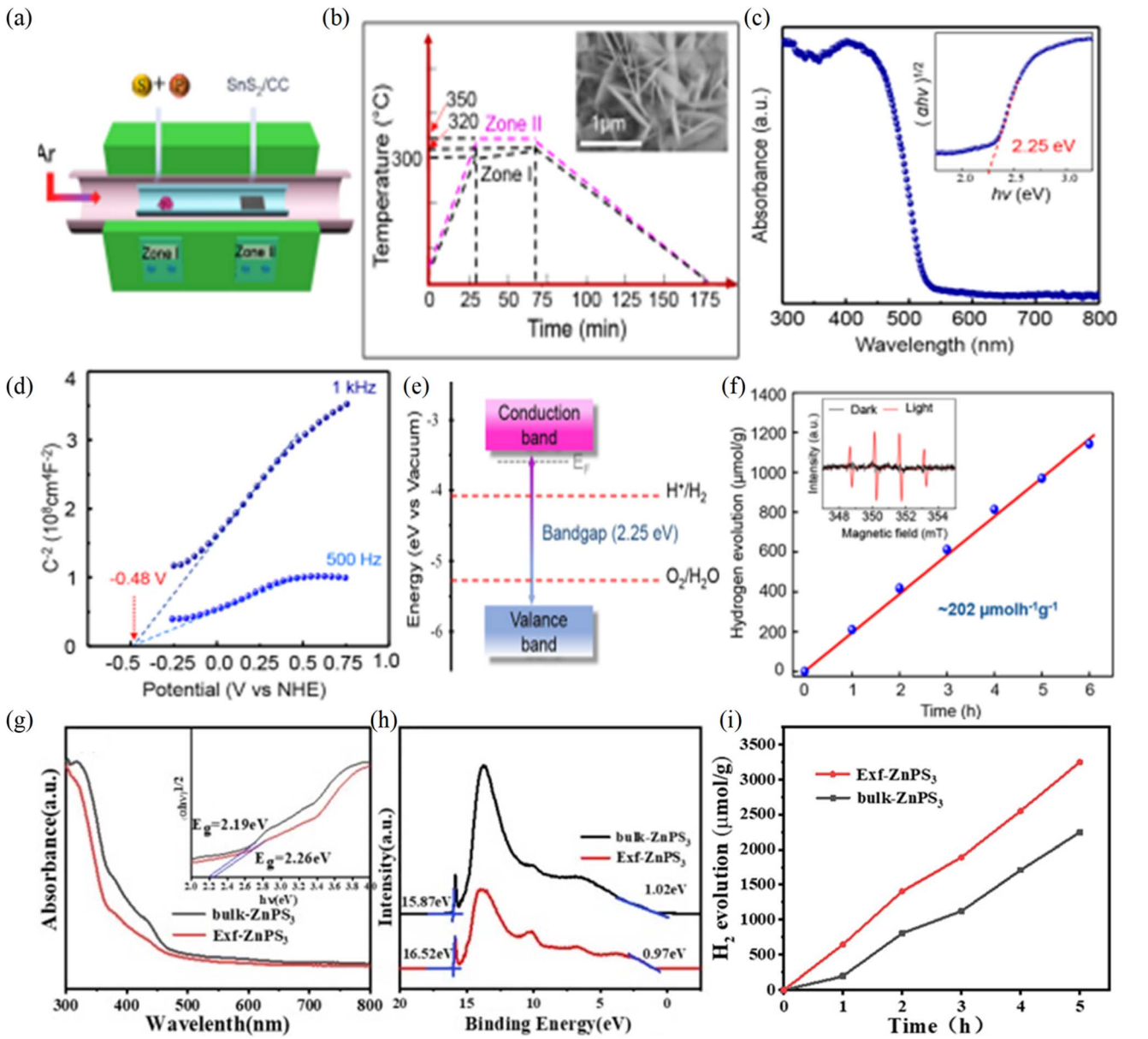

Fig. 14 (a and b) Schematic of the synthesis of $Sn_2P_2S_6$ nanosheets using a tubular furnace. UV-vis diffuse reflectance spectrum (c), Mott–Schottky plots (d), energy band diagram (e), and HER data (f) for $Sn_2P_2S_6$ nanosheets. Reprinted with permission.[111] Copyright 2021, The American Chemical Society. UV-vis extinction spectra (g), UPS spectra (h), and time course HER curves (i) for bulk and exfoliated $ZnPS_3$ catalyst. Reprinted with permission.[112] Copyright 2022, Elsevier.

$ZnPS_3$ is attributed to a high specific area and more exposed edge sites.

In 2017, Wang *et al.*[113] prepared $NiPS_3$ nanosheets by a modified CVD method and studied their HER activity under xenon light without any cocatalyst or sacrificial agent. As shown in Fig. 7g, $NiPS_3$ showed the HER activity of 26.42 μmol h^{-1} g^{-1} in neutral or pure water until the light irradiation was turned off. Further, the addition of the hole scavenger Na_2S/Na_2SO_3 to the photosystem enhanced the H_2 yield to 74.67 μmol h^{-1} g^{-1}. While the $NiPS_3$ catalyst under simulated solar light showed a lower HER activity of 6.46 μmol h^{-1} g^{-1} in the sacrificial agent-free water. The band structure of $NiPS_3$ was studied by using ultraviolet photoelectron spectroscopy and electrochemical impedance measurements indicated that the VB of $NiPS_3$ was not straddling with water oxidation potential and hence was not energetically favorable to offer holes for oxygen evolution (Fig. 7h and i). Therefore, some of the single-component MPX_3 systems utilized for photochemical HER without the cocatalyst or sacrificial agent did not evolve oxygen due to misalignment of the VB relative to the water oxidation potential. Thus, the MPX_3 catalyst also possesses the common disadvantage of the single-catalyst photosystem, wherein photoactivity decreases with time due to photocorrosion. The photogenerated electrons at CB are consumed by H^+ to generate H_2 while holes accumulate at the VB due to misalignment. These highly reactive holes further react with the semiconductor itself, which results in decomposition and reduced activity of the catalyst. Even with the presence of a sacrificial agent, the activity of $ZnPS_3$ and $NiPS_3$ nanosheets was reduced by more than half of the initial value only after 24 h of the hydrogen evolution test, which suggests deprivation in structural stability under photochemical conditions. Therefore, the activity and stability obtained with a single-component MPX_3 system are still far from reality, and photocorrosion of these materials under photocatalytic conditions impedes their applicability as photocatalysts.

In an effort to increase the H_2 evolution yield, Barua *et al.*[93] examined the photocatalytic HER activity of a range of MPX_3 systems ($MnPS_3$, $FePS_3$, $NiPS_3$, $ZnPS_3$, $CdPS_3$, $FePSe_3$, $CdPSe_3$, $Ag_{0.5}In_{0.5}PS_3$, and $Ag_{0.5}In_{0.5}PSe_3$) using eosin Y as a photosensitizer and triethanolamine (TEOA) as a sacrificial agent. This study indicated that the combination of photosensitizer and sacrificial agent somewhat assisted in extending the structural stability and long-term H_2 evolution activity. Experimentally, band gaps of all synthesized MPX_3 systems were obtained using absorption spectra and the corresponding Taucs plots revealed band gaps varied in the range of 1.29–3.3 eV, suggesting that the band gap and band edges of MPX_3 were thermodynamically suitable for the water reduction reaction. Fig. 15a shows the schematic of the probable mechanism of HER by MPX_3 compounds in the presence of Eosin Y and TEOA. Initially, the dye molecule absorbs light to yield a photoexcited dye (EY*), which then transforms to a triplet excited state (EY^3*) *via* an intersystem crossing. The intermediate EY^3* then takes an electron from TEOA *via* reductive quenching forming EY^- species. The electrons from EY^- are then transported to the CBM of the MPX_3 where H^+/H_2 reduction takes place.[97] The HER activity of monometallic TMPCs varies in the order $NiPS_3$ > $FePS_3$ > $CdPS_3$ ~ $MnPS_3$ ~ $ZnPS_3$ where $NiPS_3$ displays the highest HER rate of 2600 μmol h^{-1} g^{-1} (Fig. 15b and c). Fig. 15d presents the variation in the H_2 evolution rate of the monometallic MPX_3 with a change in P–P bond distance. The enhancement in the P–P bond distance leads to a reduction in the population of electrons at the P center, which is the active site, and therefore overall H_2 evolution rate decreases. Under similar conditions, bimetallic $Ag_{0.5}In_{0.5}PS_3$ and $Ag_{0.5}In_{0.5}PSe_3$ showed appreciable hydrogen yields of 1900 and 500 μmol h^{-1} g^{-1}, respectively (Fig. 15c). The catalytic stability is the additional significant factor for an HER catalyst. Under photochemical conditions, the $NiPS_3$ system showed steady H_2 evolution up to 5 cycles (25 h) without any decrement in H_2 evolution, suggesting long-term stability of the photocatalyst (Fig. 15e).

2D MPX_3 compounds are coupled with other semiconductors possessing good oxidation capability of holes to enhance H_2 evolution yield and avoid photocorrosion. Theoretically, Mi and coworkers[114] investigated the electronic structure of the $MnPSe_3$ heterostructure with MoS_2 using DFT calculations, where different stacking patterns of mono-layer $MnPSe_3$ with MoS_2 were investigated, as shown in Fig. 16a and b. In some stacking patterns, spin splitting at VBM of $MnPSe_3$ is evident due to the hybridization of the d orbital of Mn, which enhances electron mobility. Secondly, $MnPSe_3/MoS_2$ forms a type II heterostructure where the top of the VB is majorly contributed by $MnPSe_3$ while the bottom of CB is from MoS_2. Normally, the type I heterojunction possesses a symmetrical offset of potential barriers, where direct exciton transition occurs at the heterointerface. While in the case of type II heterojunction holes and electrons are accumulated on different sides of the heterointerface, leading to indirect exciton transition. In type II heterojunction, the spatial separation of photoexcited electrons and holes as they are localized in different sides of heterojunction, reduces the recombination rate and enhances the photocatalytic efficiency. In the case of $MnPSe_3/CrSiTe_3$ heterojunction type I heterostructure is formed due to a similar crystal structure and low lattice mismatch. However, under tensile strain the band alignment changes from type I to type II due to the transition from an indirect bandgap to a direct bandgap. The above studies demonstrated the possibility of the modulation of the electronic structure of MPX_3 by forming heterojunctions, implying the potential applicability of heterojunctions for photocatalysis applications.

Experimentally, Chen *et al.*[73] anchored 0D $Cs_4W_{11}O_{35}$ nanoparticles onto 2D $MnPS_3$ and reported higher HER yield in the case of $MnPS_3$–$Cs_4W_{11}O_{35}$ as compared to bare $MnPS_3$. 2D $MnPS_3$ is reported to be a non-toxic direct band gap semiconductor with appropriate VBM and CBM band edge potentials for photocatalytic water redox reaction. However, higher electron–hole recombination rates and their inability to oxidize water to generate oxygen limit their photo applicability. Bare $MnPS_3$ was reported to show a low H_2 production yield of 21.2 μmol h^{-1} g^{-1} under solar light illumination. To prepare $MnPS_3$–$Cs_4W_{11}O_{35}$ composites, initially, $MnPS_3$ sheets are exfoliated in NMP solvent and then tetrabutylammonium hydroxide-modified $Cs_4W_{11}O_{35}$ nanoparticles are anchored onto the

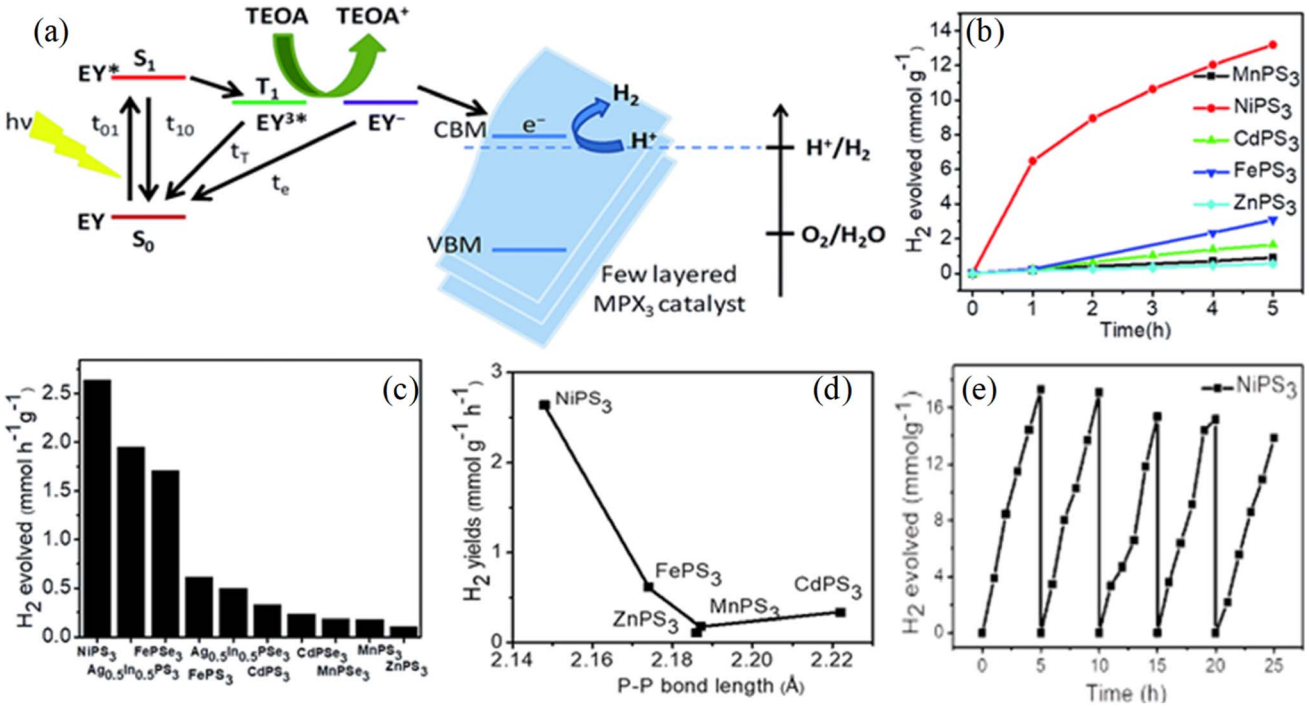

Fig. 15 (a) Schematic illustration of the mechanism of HER by exfoliated TMPCs nanosheets under a xenon lamp using eosin Y photosensitizer and TEOA sacrificial agent. (b) The yield of hydrogen evolved using monometallic ($MnPS_3$, $FePS_3$, $NiPS_3$, $ZnPS_3$, $CdPS_3$) phosphosulfides. (c) Comparison of HER activity of monometallic ($MnPS_3$, $FePS_3$, $NiPS_3$, $ZnPS_3$, $CdPS_3$ and bimetallic ($Ag_{0.5}In_{0.5}PS_3$, $Ag_{0.5}In_{0.5}PSe_3$) phosphosulfides. (d) Variation of H_2 evolution rate of monometallic phosphosulfides with p–p bond distance. (e) Cyclic stability curves for $NiPS_3$ studied up to 5 cycles for 25 h.[93]

$MnPS_3$ sheets by electrostatic interaction. The homogeneous distribution of $Cs_4W_{11}O_{35}$ nanoparticles on the $MnPS_3$ sheets *via* strong interfacial interaction of the S–W–O bond is evident in TEM images (Fig. 17a). The photocatalytic HER performance of the $MnPS_3$–$Cs_4W_{11}O_{35}$ hybrid was examined under solar light with the sacrificial Na_2S/Na_2SO_3 solution. Fig. 17b depicts the photocatalytic H_2 evolution rate of bare $MnPS_3$, $MnPS_3$–$Cs_4W_{11}O_{35}$ hybrid composites with $Cs_4W_{11}O_{35}$ mass percentages of 5.4, 10.9, and 16.5%. The H_2 evolution rates for $MnPS_3$–$Cs_4W_{11}O_{35}$ with 5.4, 10.9 and 16.5% of $Cs_4W_{11}O_{35}$ were 38, 99,

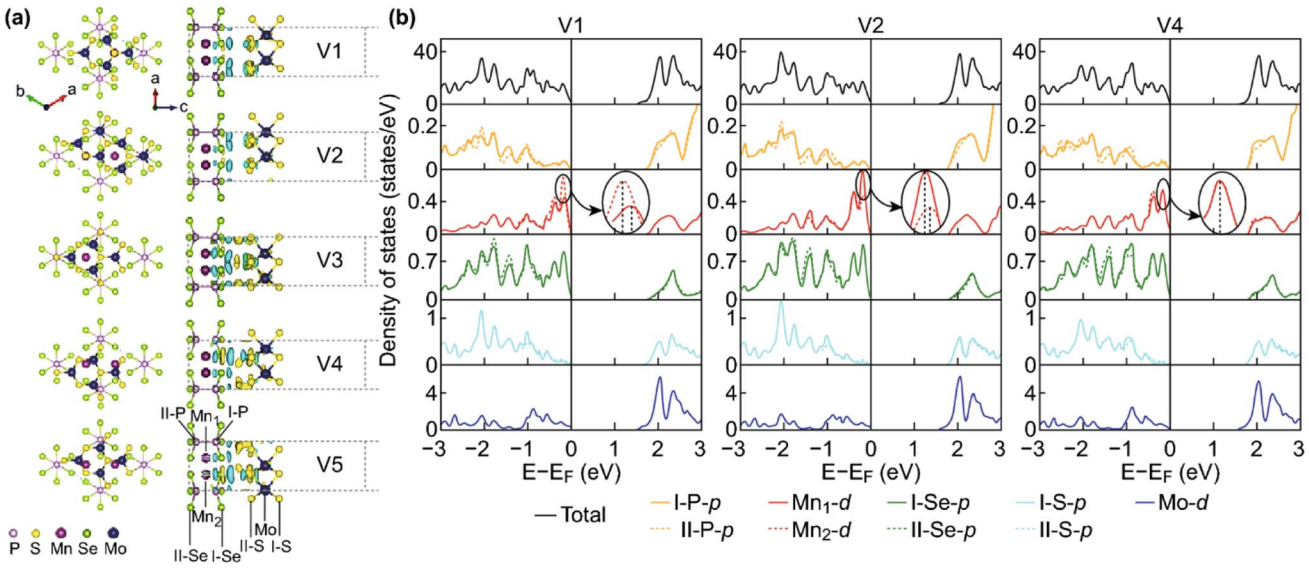

Fig. 16 (a) Structure and side view of the charge density difference of the $MnPSe_3/MoS_2$ nanocomposite with various stacking orders V1–V5. (b) Total and partial DOS of V1, V2, and V4 arrangements. The Fermi level is represented by the vertical shadow line and set to zero. Reprinted with permission.[114] Copyright 2017, Springer Nature.

and 58 μmol h^{-1} g^{-1}, respectively, while bare $MnPS_3$ showed HER activity of 21.2 μmol h^{-1} g^{-1}only. With the addition of $Cs_4W_{11}O_{35}$ nanoparticles, the photocatalytic HER activity increased first and then decreased. The maximum H_2 evolution rate of 99.6 μmol h^{-1} g^{-1} was achieved with the $MnPS_3$–$Cs_4W_{11}O_{35}$ composite with a $Cs_4W_{11}O_{35}$ mass percentage of 10.9%. In order to investigate the long-term stability of the $MnPS_3$–$Cs_4W_{11}O_{35}$ composite, photocatalytic HER experiments were performed for four cycles, and during each cycle, the quartz reactor is evacuated prior to the start of the new

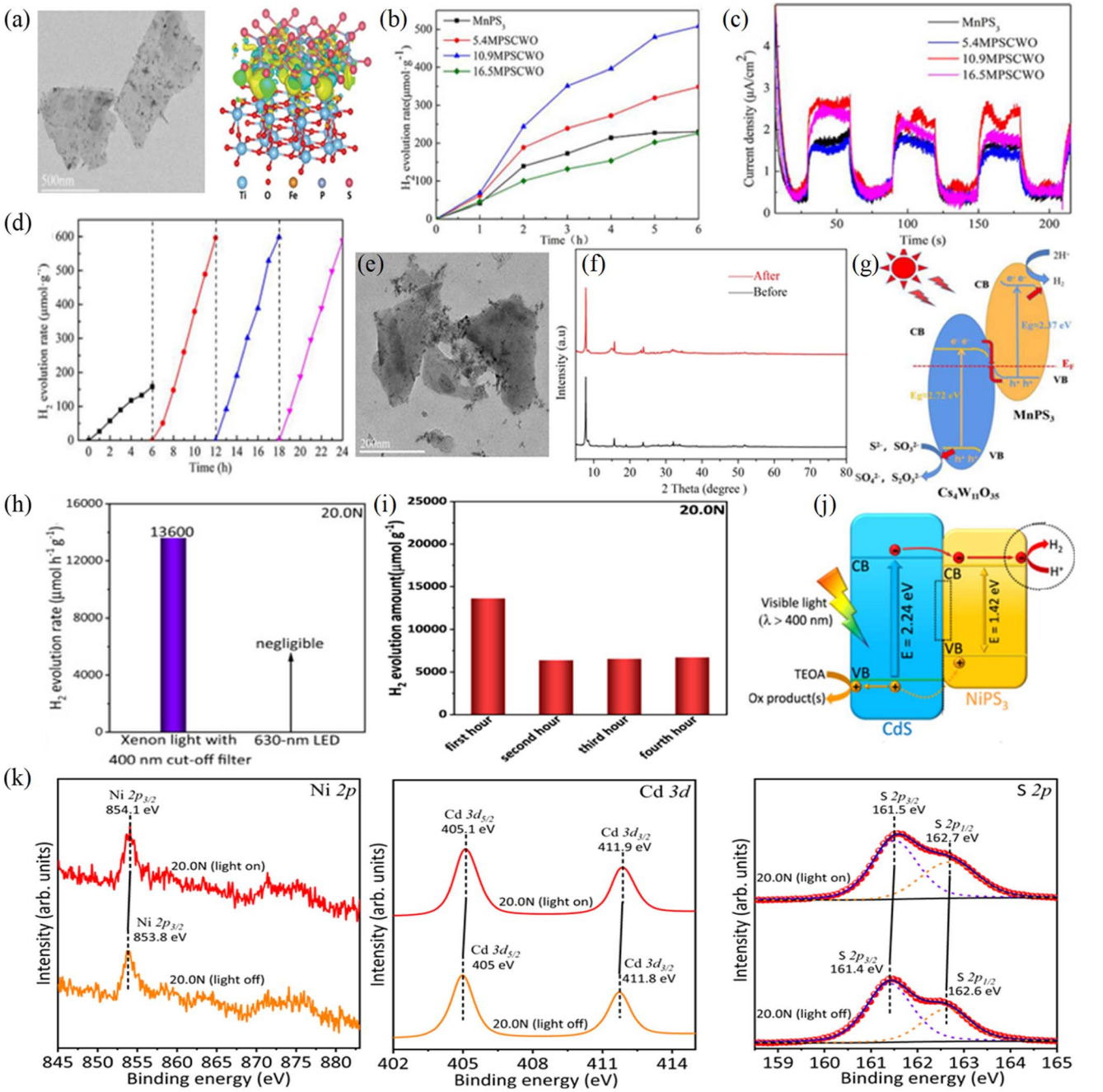

Fig. 17 (a) TEM image of the $MnPS_3$–$Cs_4W_{11}O_{35}$ heterojunction. (b and c) Time course hydrogen production data and photocurrent responses for $MnPS_3$–$Cs_4W_{11}O_{35}$ catalyst with 0, 5.4, 10.9, and 16.5% of $Cs_4W_{11}O_{35}$, and these composites designated as $MnPS_3$, 5.4MPSCWO, 10.9MPSCWO, and 16.5MPSCWO, respectively. (d) Cyclic stability curves for HER of $MnPS_3$–$Cs_4W_{11}O_{35}$ catalyst recorded for 4 cycles and 24 h. (e) TEM image of $MnPS_3$–$Cs_4W_{11}O_{35}$ after photocatalytic HER studies. (f) Raman spectra of $MnPS_3$–$Cs_4W_{11}O_{35}$ before and after photocatalytic HER studies and (g) schematic of the reaction mechanism of photocatalytic HER on Z-scheme $MnPS_3$–$Cs_4W_{11}O_{35}$ heterojunction. Adapted with permission.[73] Copyright 2021, Elsevier. (h) Time course HER curves for $NiPS_3$/CdS composite. (i) Cyclic stability curves for HER of $MnPS_3$–$Cs_4W_{11}O_{35}$ catalyst recorded for 4 h and (j) Schematic representation of generated type-I (straddling type) heterostructure between $NiPS_3$ and CdS components. (k) XPS spectra of $NiPS_3$/CdS composite with light on and off respectively. Adapted with permission.[115] Copyright 2022, Springer Nature.

experimental cycle. Cyclic stability curves shown in Fig. 17d indicate that HER activity for the second cycle is significantly higher than the first one and there is stable H_2 evolution after the second cycle. The stable H_2 evolution rate after the second cycle to the fourth cycle signifies the long-term photostability of the $MnPS_3$–$Cs_4W_{11}O_{35}$ composite. Further, TEM images of the $MnPS_3$–$Cs_4W_{11}O_{35}$ composite after photocatalytic HER studies, shown in Fig. 17e, reveal that $Cs_4W_{11}O_{35}$ nanoparticles are coupled with $MnPS_3$ sheets even after 24 h reaction. The PXRD pattern of $MnPS_3$–$Cs_4W_{11}O_{35}$ recorded after HER studies also showed that the catalyst was stable (Fig. 17f). Based on UV-vis, photoluminescence, valence band XPS spectra, and electrochemical impedance spectra studies, Chen *et al.*[60,73] proposed the formation of the Z-scheme heterojunction, which effectively suppresses the charge-hole recombination rate, charge-transfer ability, and hole oxidation ability (Fig. 17g). The internal polarization field generated due to the heterojunction formation generates more positive charges on $MnPS_3$ and more negative charges on $Cs_4W_{11}O_{35}$. Upon light irradiation, electrons and holes are produced in VB and CB of both $MnPS_3$ and $Cs_4W_{11}O_{35}$ components of the composite. Further, the internal electric field suppresses the electron transfer from CB of $Cs_4W_{11}O_{35}$ to CB $MnPS_3$ and facilitates the electron migration from CB of $Cs_4W_{11}O_{35}$ to VB of $MnPS_3$, which results in the formation of the Z-scheme heterojunction. Hence, photogenerated electrons left in the CB of $MnPS_3$ are utilized for water reduction whereas holes in the VB of $Cs_4W_{11}O_{35}$ are utilized for the oxidation of Na_2S/Na_2SO_3.

As indicated earlier, in the case of 2D $NiPS_3$, due to rapid charge recombination rate and photo-corrosion issues because of misalignment of the VBM concerning water oxidation potential, their reported HER activity is marginal. To overcome the weak oxidizing ability of $NiPS_3$, Ran *et al.*[115] coupled 2D $NiPS_3$ with 0D CdS photocatalyst, which can supply oxidative photogenerated holes rather than being utilized. Cadmium sulfide (CdS) was reported to show a narrow band gap of 2.4 eV at room temperature, which accounted for its proficient visible light absorption characteristics. Secondly, CdS possess suitable VB and CB positions for water redox reactions, which make it an excellent photocatalyst for water redox reactions. Ran *et al.* examined the photocatalytic water splitting performance of $NiPS_3$/CdS under visible-light illumination ($\lambda > 400$ nm) using TEOA as a sacrificial agent. Under light illumination, $NiPS_3$/CdS showed an extremely high H_2 evolution rate of 13 600 μmol h^{-1} g^{-1} while bare $NiPS_3$ showed negligible activity under similar conditions (Fig. 17h). The stability of $NiPS_3$/CdS for photocatalytic HER was examined for 9 h, with a cycle every 3 h. As shown in Fig. 17i, the H_2 evolution rate at cycle 3 (6687 μmol h^{-1} g^{-1}) accounted for 49.17% of that in the first cycle (13 600 μmol h^{-1} g^{-1}). This result implied the appreciable stability of the $NiPS_3$/CdS catalyst. In addition, *in situ* XPS measurements were conducted to reveal the dissociation and migration pathways of photogenerated electrons and holes on the surface of the $NiPS_3$/CdS catalyst (Fig. 17k). During the *in situ* XPS measurement, a light-emitting diode was utilized as the light source to excite the catalyst. As presented in Fig. 17k, under light irradiation Ni 2p, P 2p and S 2p signals shifted towards higher binding energy as compared to dark conditions, signifying that more photogenerated holes than electrons migrate to the surface of both $NiPS_3$ and $CdPS_3$ components. This study suggests that during photocatalysis, holes migrate to the surface and are captured by the sacrificial agent, TEOA, leaving the electrons for HER. To explain the origin of such high HER activity of the $NiPS_3$/CdS catalyst, the authors proposed a formation of type-I (straddling type) heterostructure between $NiPS_3$ and CdS based on photoluminescence, Mott–Schottky plots, ultrafast transient absorption spectroscopy, steady-state and transient-state surface photovoltage (SPV) spectroscopy studies (Fig. 17j). Upon light irradiation, electrons and holes are photogenerated in both $NiPS_3$ and CdS systems. Due to strong interfacial electronic coupling between $NiPS_3$ and CdS, the electrons and holes in CB and VB of CdS migrate to $NiPS_3$. However, most of the holes generated in CdS are consumed by sacrificial hole quencher TEOA before migrating to $NiPS_3$, resulting in the oxidation of TEOA. While a low fraction of photogenerated holes are transported from VB of CdS to VB of $NiPS_3$. On the other hand, much more photogenerated electrons in the CB of $NiPS_3$ are utilized for the water reduction reaction. The significantly high HER activity of $NiPS_3$/CdS can be attributed to the decreased recombination rate of photogenerated electron–hole pairs and abundant active sites on $NiPS_3$ for hydrogen evolution.

Xia *et al.*[116] reported the formation of S-scheme heterojunction between TiO_2 and 2D $FePS_3$ by self-assembling TiO_2 nanoparticles on $FePS_3$ nanosheets. In this study, $FePS_3/TiO_2$ nanocomposites are obtained by adding TiO_2 (P25, Degussa AG) nanoparticles to the exfoliated $FePS_3$ suspension under grinding conditions at room temperature. $FePS_3/TiO_2$ showed a higher hydrogen evolution rate of 99.5 μmol h^{-1} g^{-1} using ethanol solvent as a sacrificial electron donor under UV light illumination (Fig. 18a). While bare 2D $FePS_3$ showed negligible H_2 evolution under similar conditions. The Mott–Schottky plot for the $FePS_3/TiO_2$ composite indicated that both positive and negative slopes were obtained in distinct regions of the composite, implying the successful formation of the p–n heterojunction between 2D $FePS_3$ and TiO_2 (Fig. 18b). Further, *in situ* atomic force microscopy (AFM) combined with Kelvin probe force microscopy (AFM-KPFM) was utilized to investigate the electron transport pathway of the $FePS_3/TiO_2$ composite under light irradiation. As shown in Fig. 18d, aggregation of the TiO_2 nanoparticles on the surface of $FePS_3$ was evident in the AFM image of the $FePS_3/TiO_2$ composite. Fig. 18e and f show the corresponding KPFM images of $FePS_3/TiO_2$ in the dark and with 365 nm UV light irradiation, respectively. Accordingly, the surface potential plots of $FePS_3/TiO_2$ in dark and UV light irradiation are displayed in Fig. 18g. The surface potential across the line is enhanced under light illumination as compared to dark conditions. Particularly, the surface potential at A1 is elevated by 124 mV. This result indicated that the photogenerated holes accumulate at the surface of $FePS_3$ and TiO_2 components under light illumination. Upon light excitation, photoexcited electrons and holes are produced in both $FePS_3$ and TiO_2 components. Then, photogenerated electrons are retained in the CB of the $FePS_3$ and holes preserved in VB of TiO_2 to carry water reduction and oxidation, respectively,

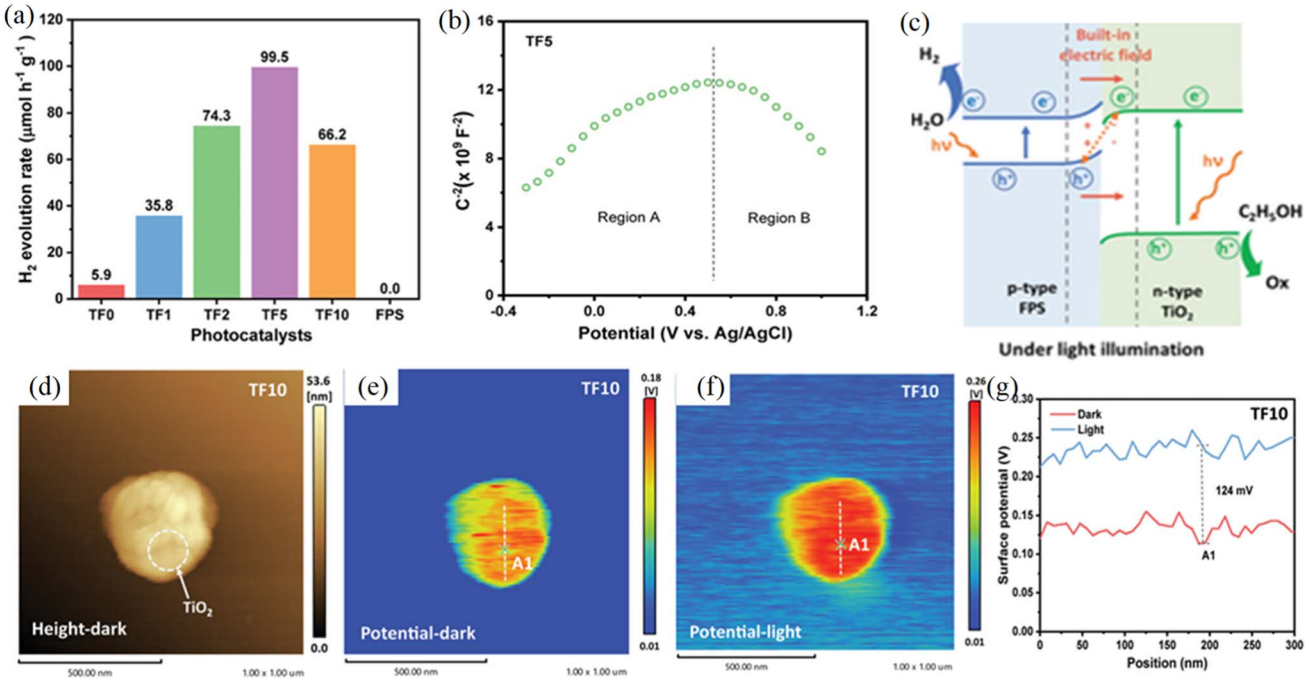

Fig. 18 (a) Photocatalytic HER activity of $FePS_3/TiO_2$ with various amounts of $FePS_3$. (b) Mott–Schottky plots for $FePS_3/TiO_2$ acquired in 0.5 M Na_2SO_4 at 3000 MHz. (c) Schematic of the reaction mechanism of photocatalytic HER on S-scheme $FePS_3/TiO_2$ components. (d and e) Atomic force microscopy (AFM) and Kelvin probe force microscopy (AFM-KPFM) image of $FePS_3/TiO_2$ in dark conditions. (f) KPFM image with UV light irradiation. (g) The corresponding surface potential plot of $FePS_3/TiO_2$ in dark and UV light irradiation. Reprinted with permission.[116] Copyright 2018, Wiley publication.

attributed to a strong in-built electric field gradient between the individual components. Meanwhile, photogenerated electrons in the VB of TiO_2 recombine with the holes in the CB of $FePS_3$. Due to the generation of the S-scheme heterojunction, the reduction ability of photogenerated electrons in $FePS_3$ and the oxidation ability of holes in TiO_2 are preserved (Fig. 18c). Secondly, a reduced recombination rate between the photogenerated electrons and holes was also simultaneously achieved. The photogenerated holes in VB of TiO_2 were utilized for the oxidation of ethanol to produce the oxidized products.

In recent years, 2D ferroelectric materials such as $CuInP_2S_6$, $CuBiP_2S_6$, and $AgInP_2Se_6$ are receiving increased attention as HER photocatalysts. The permanent polarization electric field in these materials serves as a driving force for the spatial separation of charges, thereby showing good HER activity.[117–119] Secondly, large exciton binding energy suppresses the reduction potential of the photogenerated electrons, prompting electrons readily available for the water reduction reaction. Among these MPX_3 compounds, $CuInP_2S_6$ experimentally showed good HER characteristics due to intermediate band gap and room temperature ferroelectricity.[119] Lin *et al.*[120] studied the photocatalytic HER performance of $CuInP_2S_6$, prepared by the solid-state reaction under visible light using a TEOA sacrificial electron donor. Bare $CuInP_2S_6$ nanosheets showed moderate HER activity of 18.3 μmol h^{-1} g^{-1} due to the high charge-transfer ability of the ferroelectric material. Further, the formation of 2D/2D heterojunction between $CuInP_2S_6$ and graphitic carbon nitride (g-C_3N_4) substantially accelerated the charge-transfer rate, due to which $CuInP_2S_6$/g-C_3N_4 displayed 2.5 times higher (45.1 μmol h^{-1} g^{-1}) activity than that of bare $CuInP_2S_6$ (Fig. 19a–d). Transient photocurrent response studies indicated that the composite showed a higher photocurrent density of 2.92 μA cm^{-2}, which was 1.62 and 2.25 times higher than that of individual $CuInP_2S_6$ and g-C_3N_4, respectively. This result implies the rapid charge separation and migration in the composite through high-speed microchannels. Further, photoluminescence studies implied a much lower emission intensity for the $CuInP_2S_6$/g-C_3N_4 composite compared to g-C_3N_4, indicating a much reduced electron–hole recombination rate in the composite. Based on the above results, the generation of type-II heterojunction between $CuInP_2S_6$ and g-C_3N_4 components is projected, as depicted in Fig. 19e. Upon light illumination, owing to the intrinsic dipole moment, $CuInP_2S_6$ can generate ferroelectric polarization fields with the deposition of negative and positive at opposite directions of the surface, which induces spatial charge separation. These photogenerated electrons at the $CuInP_2S_6$/g-C_3N_4 interface are utilized for water reduction to generate hydrogen, while holes are consumed by the sacrificial hole scavenger TEOA. Further, due to the in-built electric field gradient holes in the VB of g-C_3N_4 are transferred to the VB of $CuInP_2S_6$ by nanochannels, which further reduced the electron–hole recombination rate. Further, the cyclic stability curve shown in Fig. 19c implies that $CuInP_2S_6$/g-C_3N_4 still keeps high activity even after 5 cycles (15 h), suggesting their promising potential application in solar-energy conversion. In another study, Ren *et al.*[121] synthesized a $CuInP_2S_6/ZnIn_2S_4$

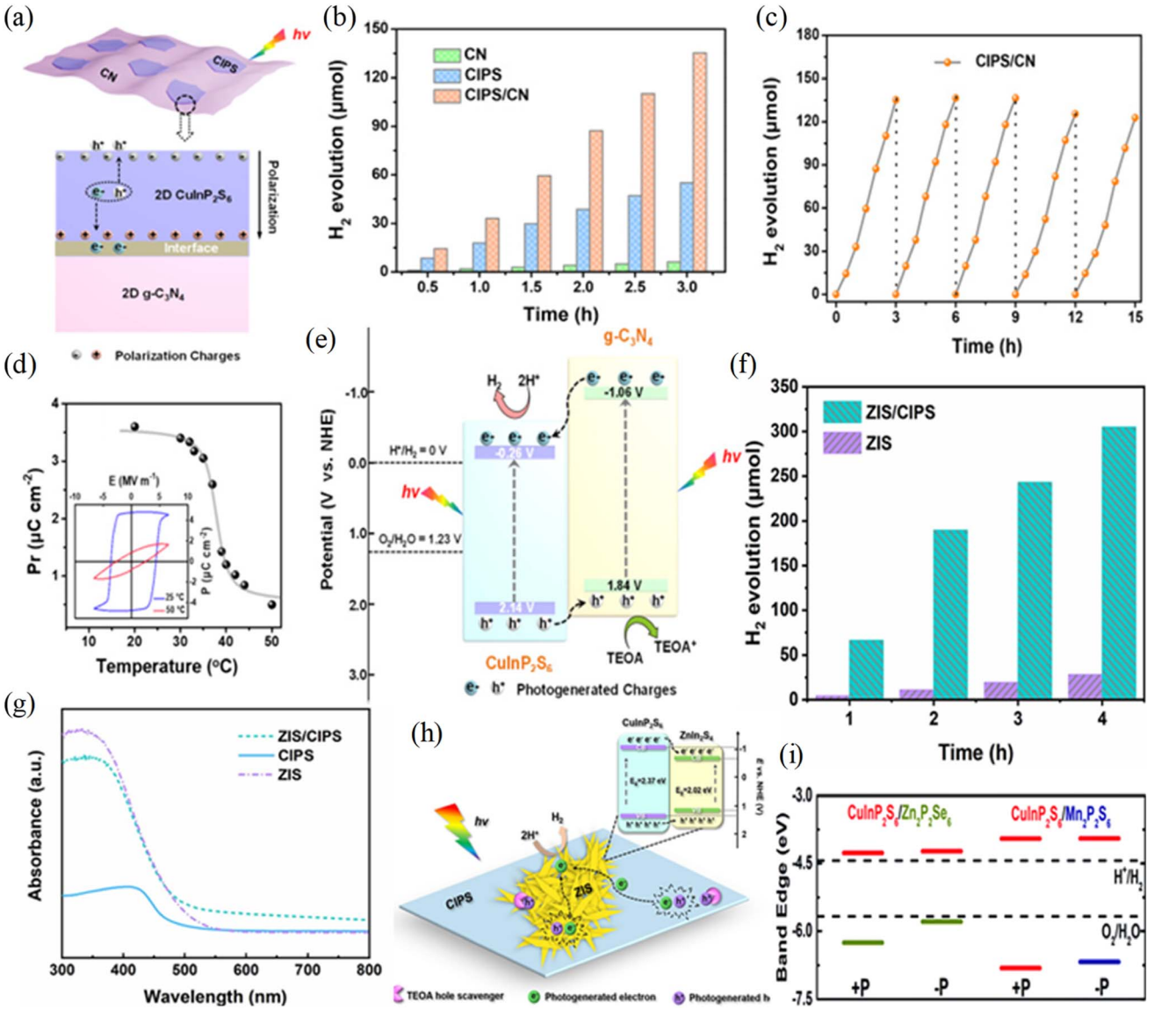

Fig. 19 (a) Schematic of the photogenerated charge carriers in 2D $CuInP_2S_6$. (b) Time course H_2 evolution data for g-C_3N_4(CN), $CuInP_2S_6$ (CIPS) and $CuInP_2S_6$/g-C_3N_4 (CN/CIPS). (c) Cyclic stability curve of HER for the $CuInP_2S_6$/g-C_3N_4 (CN/CIPS) heterojunction. (d) Temperature-dependent remnant polarization of $CuInP_2S_6$ inset: polarization-electric field (P-E) hysteresis loop obtained using piezoresponse force microscopy and (e) schematic representation of generated type-II heterostructure between $CuInP_2S_6$ and g-C_3N_4 components. Adapted with permission.[120] Copyright 2020, Elsevier. (f) Time course H_2 evolution data for $ZnIn_2S_4$ (ZIS) and $CuInP_2S_6$/$ZnIn_2S_4$ (CIPS/ZIS). (g) UV-vis diffuse reflectance spectrum of $ZnIn_2S_4$ (ZIS), $CuInP_2S_6$ (CIPS), and $CuInP_2S_6$/$ZnIn_2S_4$ (CIPS/ZIS) and (h) schematic illustration of generated type-I heterostructure at $CuInP_2S_6$/$ZnIn_2S_4$ interface. Adapted with permission.[121] Copyright 2023, Elsevier. (i) Band edge potentials of $CuInP_2S_6$/$Mn_2P_2S_6$ and $CuInP_2S_6$/$Zn_2P_2Se_6$ ferroelectric heterostructures obtained using DFT+U method. The HER and OER potentials are shown for comparison. +P and −P designate $CuInP_2S_6$ in two oppositely polarized states.[119]

heterostructure by a surfactant-assisted hydrothermal method and utilized it for photocatalytic H_2 generation. As shown in Fig. 19f, bare $ZnIn_2S_4$ showed a quite inferior H_2 evolution rate of 5.88 μmol h^{-1} g^{-1}, while $CuInP_2S_6$/$ZnIn_2S_4$ displayed an enhanced activity of 76.2 μmol h^{-1} g^{-1}. The band gap energy values for $CuInP_2S_6$ and $ZnIn_2S_4$ estimated using a UV-vis diffuse reflectance study were 2.37 and 2.02 eV, respectively (Fig. 19g). Owing to the matched band gap energy value between $CuInP_2S_6$ and $ZnIn_2S_4$, a type I heterostructure was effectively generated, which led to the efficient separation of the photogenerated electrons and holes (Fig. 19h). On visible-light irradiation, photogenerated electrons in the CB of $CuInP_2S_6$ migrated to the CB of $ZnIn_2S_4$ at the interface and were utilized for H^+ reduction to yield H_2. While photogenerated holes in the VB of $CuInP_2S_6$ migrated to the VB of $ZnIn_2S_4$ and were finally captured by the sacrificial agent TEOA. Markedly, due to the generation of the heterostructure, abundant charge-migration pathways were created, which reduced the charge recombination rate and improved the HER yield.

Theoretically, Huang *et al.*[119] projected that the generation of ferroelectric hetero-interfaces such as $CuInP_2S_6$/$Mn_2P_2S_6$ and $CuInP_2S_6$/$Zn_2P_2Se_6$ would be beneficial for photocatalytic water

splitting due to strong visible light absorption and type-II band alignment, which can facilitate rapid charge separation (Fig. 19i). To date, there are very limited experimental studies on ferroelectric hetero-interfaces containing 2D MPX_3 compounds for photocatalysis and these systems need to be investigated in more detail. In Table 2, we have listed the photocatalytic HER activity of various 2D metal thiophosphates and their heterostructures reported in the literature along with the reaction conditions. It should be noted that, while comparing the HER activity between two individual systems, the strength of the light source (simulated solar light or xenon lamp, 300 W or 400 W), photosensitizer added and type of sacrificial agent (TEOA and Na_2S/Na_2SO_3) need to be taken into consideration since these factors can affect the activity significantly. Secondly, different synthetic approaches generate MPX_3 layers of various thicknesses, which further affect the HER activity as accessibility for catalytic edge (active) sites decreases with an increase in the layer thickness.

Among the reported various 2D MPX_3 compounds, $CdPS_3$ showed a significantly high H_2 evolution rate of 10 880 μmol h^{-1} g^{-1}, while $CuPS_3$ and $ZnPS_3$ displayed 2085 and 640 μmol h^{-1} g^{-1}, respectively (Table 1). However, in a single-component MPX_3 system, the photogenerated holes are confined to the semiconductor and not available for water oxidation, hence resulting in photocorrosion of the semiconductor. The combination of sacrificial hole scavengers such as Na_2S/Na_2SO_3 or triethanolamine with 2D MPX_3 alleviates photocorrsion, and increases the activity to some extent. Generally, the formation of hetero-interfaces between 2D MPX_3 compounds and material with good oxidation capability for holes such as $Cs_4W_{11}O_{35}$ and

Table 2 Comparison of photocatalytic HER activity of 2D TMPCs and their nanocomposites with $Cs_4W_{11}O_{35}$, CdS, TiO_2, and g-C_3N_4

Photocatalyst system	Synthesis method, layer thickness	Light source	Sacrificial agent	HER activity (μmol h^{-1} g^{-1})	Ref.
$MnPS_3$	CVD[a], 6 nm	AM 1.5G[b]	—	3.1	55
$MnPS_3$	CVD, 6 nm	AM 1.5G	Na_2S/Na_2SO_3	21.2	55
$MnPSe_3$	CVD, 28 nm	AM 1.5G	—	6.5	55
$MnPSe_3$	CVD, 28 nm	AM 1.5G	Na_2S/Na_2SO_3	43.5	55
$FePS_3$	CVD, 20 nm	300 W Xe lamp	$FeSO_4$	46.6	131
$FePS_3$	CVD, 20 nm	300 W Xe lamp	Triethanolamine	141.9	131
$FePS_3$	CVD, 20 nm	300 W Xe lamp	Na_2S/Na_2SO_3	402.4	131
$FePS_3$	SS method[c]	300 W Xe lamp	Triethanolamine	166.2	132
$FePS_3$	LPE[d],10 nm	300 W Xe lamp	Triethanolamine	290.0	133
Porous $FePS_3$	SS 7 nm	300 W Xe lamp	Triethanolamine	305.6	132
$NiPS_3$	CVD, 3.5 nm	AM 1.5G	—	26.42	113
$NiPS_3$	CVD, 3.5 nm	AM 1.5G	Na_2S/Na_2SO_3	74.67	113
$CuPS_3$	Hot injection	150W simulator	Na_2S/Na_2SO_3	2085	63
$ZnPS_3$	LPE	300 W Xe lamp	Na_2S/Na_2SO_3	640.0	112
$CdPS_3$	CVD	AM 1.5G	Na_2S/Na_2SO_3	786.6	131
$CdPS_3$	LPE, 3 nm	300 W Xe lamp	Ethanol	10 880.0	71
N-doped $CdPS_3$	LPE	300 W Xe lamp	DL-lactic acid	6280.0	134
$InPS_3$	CVD	AM 1.5G	Na_2S/Na_2SO_3	379.1	131
$Sn_2P_2S_6$	CVD	AM 1.5G	Na_2S/Na_2SO_3	202.06	135
$ZnIn_2S_4$	SS method	Visible light ($\lambda \geq 420$ nm)	—	5.88	121
2D MPX_3 HER activity reported with photosensitizer eosin Y (EY)					
EY/$MnPS_3$	LPE	400 W Xe lamp	Triethanolamine	200.0	93
EY/$FePS_3$	LPE	400 W Xe lamp	Triethanolamine	600.0	93
EY/$NiPS_3$	LPE, 4.9 nm	400 W Xe lamp	Triethanolamine	2600.0	93
EY/$ZnPS_3$	LPE	400 W Xe lamp	Triethanolamine	100.0	93
EY/$CdPS_3$	LPE	400 W Xe lamp	Triethanolamine	300.0	93
EY/$MnPSe_3$	LPE	400 W Xe lamp	Triethanolamine	200.0	93
EY/$FePSe_3$	LPE, 6.2 nm	400 W Xe lamp	Triethanolamine	1700.0	93
EY/$CdPSe_3$	LPE	400 W Xe lamp	Triethanolamine	200.0	93
EY/$Ag_{0.5}In_{0.5}PS_3$	LPE, 2.1 nm	400 W Xe lamp	Triethanolamine	1900.0	93
EY/$Ag_{0.5}In_{0.5}PS_3$	LPE, 3.1 nm	400 W Xe lamp	Triethanolamine	500.0	93
2D MPX_3 heterojunctions					
$MnPS_3/Cs_4W_{11}O_{35}$	—	300 W Xe lamp	Na_2S/Na_2SO_3	99.0	73
$NiPS_3$/CdS	—	300 W Xe lamp	Triethanolamine	13 600.0	64
$FePS_3/TiO_2$	—	350 W Xe lamp	Ethanol	99.5	116
$MnPS_3$/carbon dot	—	300 W Xe lamp	—	339.63	136
$CuInP_2S_6$	—	300 W Xe lamp	Triethanolamine	18.3	120
$CuInP_2S_6$/g-C_3N_4	—	300 W Xe lamp	Triethanolamine	45.1	120
$CuInP_2S_6/ZnIn_2S_4$	SS method	Visible light ($\lambda \geq 420$ nm)	—	76.2	121

[a] CVD – chemical vapor deposition. [b] AM 1.5G – simulated solar light. [c] SS – solid state method. [d] LPE – liquid phase exfoliation.

Table 3 Comparison of photocatalytic HER activity of mono and bimetallic 2D TMPCs and their nanocomposites with other 2D material naocomposites reported in the literature

2D nanomaterials							
				Cyclic stability			
Photocatalyst system	Light source	Sacrificial agent	HER activity (μmol h^{-1} g^{-1})	No. of cycles	Total time of cycle (h)	HER activity after cyclic stability as compared with 1st cycle	References
C_3N_4	300 W Xe lamp	TEOA[a]	169.5	4	20	Negligible change	137
MoS_2	300 W Xe lamp	TEOA	339.5	—	—	NR[b]	138
$ZnInS_4$	300 W Xe lamp	Na_2S/Na_2SO_3	3890.0	3	9	Negligible change	139
CdS	300 W Xe lamp	MeOH	370.0	—	—	NR	140
$FeSe_2$	300 W Xe lamp	Na_2S/Na_2SO_3	955.3	—	—	NR	141
Fe–BiOCl	300 W Xe lamp	Na_2SO_4	3540.0	—	—	NR	142
Phosphorene	300 W Xe lamp	Na_2S/Na_2SO_3	512.0	2	20	Negligible change	143
$CuPS_3$[c]	150W simulator	Na_2S/Na_2SO_3	2085.0	3	24	Negligible change	63
EY/$NiPS_3$[c,d]	400 W Xe lamp	TEOA	2600.0	5	25	Negligible change	93
$CdPS_3$[c]	300 W Xe lamp	Ethanol	10 880.0	—	—	NR	71
2D nanomaterial-based heterostructures							
MoS_2/CdS	300 W Xe lamp	Lactic acid	4060.0	3	15	Negligible change	144
MoS_2/TiO_2	300 W Xe lamp	TEOA	10 046.0	3	12	Negligible change	145
MoS_2/C_3N_4	300 W Xe lamp	TEOA	1155.0	3	12	1098 μmol h^{-1} g^{-1}	146
MoS_2/C_3N_4	AM 1.5G	TEOA	8300.0	6	16	Negligible change	147
Ti_3C_2/CdS	530 W Xenon lamp	MeOH	1730.0	3	18	Negligible change	140
$Cu_3P/ZnInS_4$	300 W Xe lamp	TEOA	5461.0	6	18	Negligible change	148
WS_2/CdS	400 W Xe lamp	Lactic acid	13 132.0	4	12	Negligible change	149
$FeSe_2/C_3N_4$	300 W Xe lamp	Na_2S/Na_2SO_3	1655.6	2	12	Negligible change	141
Ti_3C_2/TiO_2	300 W Xe lamp	MeOH	4672.0	5	25	Negligible change	150
C_3N_4/phosphorene	300 W Xe lamp	TEOA	5850.0	3	12	Negligible change	151
$MnPS_3/Cs_4W_{11}O_{35}$[c]	300 W Xe lamp	Na_2S/Na_2SO_3	99.0	4	24	Negligible change	73
$NiPS_3/CdS$[c]	300 W Xe lamp	TEOA	13 600.0	4	4	6800 μmol h^{-1} g^{-1}	64

[a] TEOA – triethanolamine. [b] NR – not reported. [c] 2D phosphochalcogenides. [d] EY – eosin Y dye.

CdS enhances the HER yield and photostability of 2D $MnPS_3$. The combination of $NiPS_3$ and $FePS_3$ with CdS and TiO_2 appears to be advantageous for photocatalytic HER. Mainly, the $NiPS_3$/CdS heterostructure displayed a significantly high H_2 evolution rate of 13 600 μmol h^{-1} g^{-1}. The generation of heterojunction effectively suppresses the electron–hole recombination rate and improves the charge-transfer and hole oxidation ability due to the internal polarization field. In Table 3, we have compared the photocatalytic HER activity of 2D MPX_3 nanocomposites with other 2D materials (C_3N_4, metal sulfides, phosphides, and carbides) and their nanocomposites reported in the literature. The HER activity obtained with $NiPS_3$/CdS surpasses the highest reported for TMDCs-based nanocomposites, indicating that 2D MPX_3-based composites could be beneficial for large-scale hydrogen production with exceptional stability.

6. Conclusions and future opportunities

The global energy crisis and environmental pollution problems have become increasingly severe and the search for clean and sustainable energy resources is vital. Water splitting utilizing solar energy, electrical energy, or a combination of solar-electrical energy is demonstrated to be the environment-friendly route for future green hydrogen production. From the practical application viewpoint, designing a high-performance and cost-effective, yet metal-free catalyst, for photocatalytic/electrocatalytic water splitting is technologically essential and urgently needed.

In this perspective, we discussed the recent development of non-noble metal catalysts for water-splitting reactions with a focus on 2D MPX_3 compounds by emphasizing novel strategies developed for activating MPX_3 for photocatalytic and electrocatalytic HER. Theoretically, Gibbs free energy of hydrogen adsorption is considered to be a good descriptor in evaluating HER performance, and material with an approximate ΔG_H value of zero is considered to be an ideal catalyst. DFT calculations revealed that pyrite type CoPS shows thermoneutral H^+ adsorption, and also experimentally substantiated that CoPS possess Pt/C-like electrocatalytic H_2 evolution activity. The exfoliation of bulk MPX_3 into thin sheets enhances the HER activity due to the increased in-plane conductivity and more exposed edge sites. The electronic conductivity and HER activity

of MPS_3 sheets can be further improved by coupling a conducting matrix such as graphene. Doping of Co atoms into $FePS_3$ and $NiPS_3$ systems also enhances HER kinetics due to the electronic state modulation with doping. Coupling of TMPCs with other 2D systems such as MoS_2 facilitates hydrogen spillover during H_2 evolution from the MoS_2 edge site to MPX_3. These MPX_3/MoS_2 composites also showed good OER characteristics, indicating that these composites can be useful for overall water-splitting applications.

Strong visible light absorption characteristics, high carrier mobility, and thermoneutral H^+ adsorption of 2D MPX_3 make them suitable catalysts for photocatalytic water splitting. However, single-component MPX_3 as a photocatalyst showed marginal HER activity and low stability due to misaligned VBM with respect to water oxidation potential. The development of MPX_3 for photocatalytic HER is presently concentrating on enhancing the light absorption efficiency, the alleviation of photocorrosion, industrial scale H_2 production, and improving stability. The addition of sacrificial hole scavengers such as Na_2S/Na_2SO_3 or triethanolamine alleviates photocorrsion, and increases the activity and stability to some extent. Nevertheless, band gap engineering is required to enhance light absorption and reduce the photogenerated electron–hole recombination rate.

By coupling $MnPS_3$ with a $Cs_4W_{11}O_{35}$ semiconductor possessing good oxidation capability of holes, the HER activity of individual components can be enhanced. The generation of Z-scheme heterojunction between $MnPS_3$ and $Cs_4W_{11}O_{35}$ effectively suppresses the electron–hole recombination rate and improves charge-transfer and hole oxidation ability due to the internal polarization field. Further, a combination of $NiPS_3$ and $FePS_3$ with CdS and TiO_2, respectively appears to be advantageous for photocatalytic HER. Particularly, the $NiPS_3$/CdS heterojunction showed superior HER activity of 13 600 $\mu mol\ h^{-1}\ g^{-1}$, which is comparable to that of some of the highest reported transition metal-based nanocomposites reported in the literature.

In spite of the overwhelming progress in photocatalysis/electrocatalysis of 2D MPX_3, there is still a lot of scope to enhance the performance and stability towards commercialization, some points are listed below.

6.1 Synthesis of atomically thin 2D MPX_3 nanosheets

The chemical vapor transport method is the most widely utilized strategy to obtain bulk MPX_3 and is then converted to a few-layer form by liquid-phase exfoliation. Most of the liquid-phase exfoliation strategies yield few-layer MPX_3 nanosheets, which are semiconducting in nature. In the case of MoS_2, lithium-intercalation of bulk material is exploited to produce atomically-thin metallic 2D sheets on a large scale. However, the lithium-intercalation approach in preparing atomically-thin MPX_3 is not reported and these exfoliated can show enhanced HER characteristics if they are converted to the metallic form due to the increased in-plane conductivity and exposed edge sites. Further, the crystal structure and HER properties of these exfoliated systems need to be optimized with combined theoretical and experimental work to maximize their catalytic efficiency.

6.2 Surface functionalization

Similar to TMDCs, most of the 2D MPX_3 systems show poor ambient stability due to reactive sulfur and phosphorous atoms. Covalent functionalization with electron-donating and withdrawing moieties can enhance the ambient stability and dispersibility of 2D MPX_3, which is crucial for catalysis applications. Secondly, surface functionalization can improve the hydrogen adsorption/desorption ability of 2D MPX_3 under various electrolytic conditions. The generation of heterojunction between functionalized 2D MPX_3 with other 2D materials using covalent cross-linking or electro-restacking strategies could further improve charge-transfer characteristics and expose edge sites for HER.

6.3 Doping of non-metal atoms

Doping metal atoms of 2D MPX_3 with other transition elements to form bimetallic compounds improves the HER characteristics through the electronic state modulation. However, a very limited reports on doping P and S/Se species, and these sites are reported to be active for hydrogen adsorption and desorption during HER. Therefore, controlled doping of non-metal elements, such as N and O can alter the electron donating/withdrawing ability of the active site, thereby improving HER characteristics. Secondly, co-doping of metal and non-metal elements would give rise to synergistic interactions. Theoretical insights of co-doping to modulate the electronic structure will assist experimental studies to tailor the transport properties of the system.

6.4 Ternary and mixed dimensional heterostructures

The generation of a ternary heterostructure of graphene, 2D MPX_3, and layered double hydroxides (LDHs)/MXenes is worth exploring for overall water splitting as this system possesses optimum HER and OER sites with good electronic conductivity. It is important to note that some of the MPX_3 systems, which show high HER activity suffer from issues related to stability and *vice versa*. In the case of a ternary superlattice-like structure, the 2D MPX_3 layer is sandwiched between other 2D components, which can improve the structural and catalytic stability along with the activity. Further, coupling of 2D TMPCs with other 1D carbon nanotubes or with 1D MoS_2 can generate a 3D porous framework with more accessibility for electrolytes, highly exposed edge sites, and interconnected electron-transfer channels, which will be useful for other HER-related catalysis applications.

After potential developments of proficient H_2 evolution catalysts, recent research has demonstrated that 2D MPX_3 catalysts can be highly efficient for photocatalytic and electrocatalytic water splitting. Solar water-splitting reactors need to be established to sustain large-scale H_2 production at a low cost. In this context, photoelectrochemical cells (PECs) have the benefit of exploiting both solar and electrical energy and concurrently separating evolved H_2 from O_2. Band gap tunability and good

electronic conductivity make 2D MPX_3 a potential candidate for HER with high solar-to-hydrogen conversion efficiency. Also, strategies for safe H_2 storage and transport need to be developed.

Conflicts of interest

The authors declare no conflicts of interest.

Acknowledgements

K. Pramoda gratefully acknowledges financial assistance from Science and Engineering Research Board, Government of India, Start-up Research Grant No. SRG/2022/000988, Vision Group on Science and Technology, Karnataka Science and Technology Promotion Society, Government of Karnataka (No. KSTePS/VGST/2021-22/CISEE/GRD-1010/66/2022-23/33) and the Minor Research Project Grant, Jain University (No. JU/MRP/CNMS/30/2023).

References

1 R. Eisenberg, *Science*, 2009, **324**, 44–45.
2 X. Tao, Y. Zhao, S. Wang, C. Li and R. Li, *Chem. Soc. Rev.*, 2022, **51**, 3561–3608.
3 Y. Wang, H. Suzuki, J. Xie, O. Tomita, D. J. Martin, M. Higashi, D. Kong, R. Abe and J. Tang, *Chem. Rev.*, 2018, **118**, 5201–5241.
4 A. Kudo and Y. Miseki, *Chem. Soc. Rev.*, 2009, **38 1**, 253–278.
5 I. Staffell, D. Scamman, A. Velazquez Abad, P. Balcombe, P. E. Dodds, P. Ekins, N. Shah and K. R. Ward, *Energy Environ. Sci.*, 2019, **12**, 463–491.
6 D. A. Cullen, K. C. Neyerlin, R. K. Ahluwalia, R. Mukundan, K. L. More, R. L. Borup, A. Z. Weber, D. J. Myers and A. Kusoglu, *Nat. Energy*, 2021, **6**, 462–474.
7 R. M. Ormerod, *Chem. Soc. Rev.*, 2003, **32**, 17–28.
8 L. Fan, Z. Tu and S. H. Chan, *Energy Rep.*, 2021, **7**, 8421–8446.
9 M. K. Singla, P. Nijhawan and A. S. Oberoi, *Environ. Sci. Pollut. Res.*, 2021, **28**, 15607–15626.
10 P. E. Dodds, I. Staffell, A. D. Hawkes, F. Li, P. Grünewald, W. McDowall and P. Ekins, *Int. J. Hydrogen Energy*, 2015, **40**, 2065–2083.
11 A. Roy, M. Chhetri and C. N. R. Rao, in *Advances in the Chemistry and Physics of Materials*, 2019, pp. 376–398, DOI: **10.1142/9789811211331_0016**.
12 K. Pramoda and C. N. R. Rao, *APL Mater.*, 2023, **11**, 020901.
13 U. Maitra, U. Gupta, M. De, R. Datta, A. Govindaraj and C. N. R. Rao, *Angew. Chem., Int. Ed. Engl.*, 2013, **52**, 13057–13061.
14 Y. R. Girish, Udayabhanu, N. M. Byrappa, G. Alnaggar, A. Hezam, G. Nagaraju, K. Pramoda and K. Byrappa, *J. Hazard. Mater. Adv.*, 2023, **9**, 100230.
15 M. G. Walter, E. L. Warren, J. R. McKone, S. W. Boettcher, Q. Mi, E. A. Santori and N. S. Lewis, *Chem. Rev.*, 2010, **110**, 6446–6473.
16 K. Takanabe, *ACS Catal.*, 2017, **7**, 8006–8022.
17 Z. Li, M. Hu, P. Wang, J. Liu, J. Yao and C. Li, *Coord. Chem. Rev.*, 2021, **439**, 213953.
18 L. Sun, Q. Luo, Z. Dai and F. Ma, *Coord. Chem. Rev.*, 2021, **444**, 214049.
19 K. Pramoda, S. Servottam, M. Kaur and C. N. R. Rao, *ACS Appl. Nano Mater.*, 2020, **3**, 1792–1799.
20 N. Cheng, S. Stambula, D. Wang, M. N. Banis, J. Liu, A. Riese, B. Xiao, R. Li, T.-K. Sham, L.-M. Liu, G. A. Botton and X. Sun, *Nat. Commun.*, 2016, **7**, 13638.
21 K. Li, Y. Li, Y. Wang, J. Ge, C. Liu and W. Xing, *Energy Environ. Sci.*, 2018, **11**, 1232–1239.
22 M. Chhetri, S. Sultan and C. N. R. Rao, *Proc. Natl. Acad. Sci. U. S. A.*, 2017, **114**, 8986–8990.
23 M. Chhetri, S. Maitra, H. Chakraborty, U. Waghmare and C. N. R. Rao, *Energy Environ. Sci.*, 2016, **9**, 95–101.
24 K. Pramoda, U. Gupta, M. Chhetri, A. Bandyopadhyay, S. K. Pati and C. N. R. Rao, *ACS Appl. Mater. Interfaces*, 2017, **9**, 10664–10672.
25 L. Yu, Q. Zhu, S. Song, B. McElhenny, D. Wang, C. Wu, Z. Qin, J. Bao, Y. Yu, S. Chen and Z. Ren, *Nat. Commun.*, 2019, **10**, 5106.
26 D. C. Binwal, K. Pramoda, A. Zak, M. Kaur, P. Chithaiah and C. N. R. Rao, *ACS Appl. Energy Mater.*, 2021, **4**, 2339–2347.
27 U. Gupta and C. N. R. Rao, *Nano Energy*, 2017, **41**, 49–65.
28 M. M. Ayyub, R. Singh and C. N. R. Rao, *Sol. RRL*, 2020, **4**, 2000050.
29 Y. R. Girish, K. Jaiswal, P. Prakash and M. De, *Catal. Sci. Technol.*, 2019, **9**, 1201–1207.
30 K. Pramoda, D. C. Binwal and C. N. R. Rao, *Mater. Res. Bull.*, 2022, **149**, 111697.
31 Y.-W. Cheng, J.-H. Dai, Y.-M. Zhang and Y. Song, *J. Phys. Chem. C*, 2018, **122**, 28113–28122.
32 Y. Abghoui and E. Skúlason, *J. Phys. Chem. C*, 2017, **121**, 24036–24045.
33 C. Hu, C. Lv, S. Liu, Y. Shi, J. Song, Z. Zhang, J. Cai and A. Watanabe, *Catalysts*, 2020, **10**, 188.
34 X. Xu, H. Xu and D. Cheng, *Nanoscale*, 2019, **11**, 20228–20237.
35 C. Tsai, F. Abild-Pedersen and J. K. Nørskov, *Nano Lett.*, 2014, **14**, 1381–1387.
36 X. Tan, D. Zhao, Y. Sun, Z. Duan, X. Wang and X. Wu, *CrystEngComm*, 2022, **24**, 6696–6704.
37 X. Dai, K. Du, Z. Li, M. Liu, Y. Ma, H. Sun, X. Zhang and Y. Yang, *ACS Appl. Mater. Interfaces*, 2015, **7**, 27242–27253.
38 D. Mosconi, P. Till, L. Calvillo, T. Kosmala, D. Garoli, D. Debellis, A. Martucci, S. Agnoli and G. Granozzi, *Surfaces*, 2019, **2**, 531–545.
39 D. C. Binwal, M. Kaur, K. Pramoda and C. N. R. Rao, *Bull. Mater. Sci.*, 2020, **43**, 313.
40 B. Konkena, J. Masa, W. Xia, M. Muhler and W. Schuhmann, *Nano Energy*, 2016, **29**, 46–53.
41 J. Wang, X. Yue, Y. Yang, S. Sirisomboonchai, P. Wang, X. Ma, A. Abudula and G. Guan, *J. Alloys Compd.*, 2019, **819**, 153346.
42 C. C. Weng, J.-T. Ren and Z. Yuan, *ChemSusChem*, 2020, **13**, 3357–3375.

43 L. Chen, J.-T. Ren and Z.-Y. Yuan, *Green Chem.*, 2022, **24**, 713–747.
44 H. Zhang, T. Wei, Y. Qiu, S. Zhang, Q. Liu, G. Hu, J. Luo and X. Liu, *Small*, 2023, **19**, 2207249.
45 J. Jia, W. Zhou, G. Li, L. Yang, Z. Wei, L. Cao, Y. Wu, K. Zhou and S. Chen, *ACS Appl. Mater. Interfaces*, 2017, **9**, 8041–8046.
46 M. Cabán-Acevedo, M. L. Stone, J. R. Schmidt, J. G. Thomas, Q. Ding, H.-C. Chang, M.-L. Tsai, J.-H. He and S. Jin, *Nat. Mater.*, 2015, **14**, 1245–1251.
47 D. Mukherjee, P. M. Austeria and S. Sampath, *ACS Energy Lett.*, 2016, **1**, 367–372.
48 S. Wang, B. Xiao, S. Shen, K. Song, Z. Lin, Z. Wang, Y. Chen and W. Zhong, *Nanoscale*, 2020, **12**, 14459–14464.
49 K. Li, D. Rakov, W. Zhang and P. Xu, *Chem. Commun.*, 2017, **53**, 8199–8202.
50 H. Huang, J. Song, D. Yu, Y. Hao, Y. Wang and S. Peng, *Appl. Surf. Sci.*, 2020, **525**, 146623.
51 Y. Liu, Y. Chen, Y. Tian, T. Sakthivel, H. Liu, S. Guo, H. Zeng and Z. Dai, *Adv. Mater.*, 2022, **34**, 2203615.
52 J. Yang, D. Wang, H. Han and C. Li, *Acc. Chem. Res.*, 2013, **46**, 1900–1909.
53 T. Hisatomi, J. Kubota and K. Domen, *Chem. Soc. Rev.*, 2014, **43**, 7520–7535.
54 M. A. Nadeem, M. A. Khan, A. A. Ziani and H. Idriss, *Catalysts*, 2021, **11**, 60.
55 J. Ran, J. Zhang, J. Yu, M. Jaroniec and S. Z. Qiao, *Chem. Soc. Rev.*, 2014, **43**, 7787–7812.
56 K. Pramoda and C. N. R. Rao, *ChemNanoMat*, 2022, **8**, e202200153.
57 A. Fujishima and K. Honda, *Nature*, 1972, **238**, 37–38.
58 K. Maeda, *J. Photochem. Photobiol., C*, 2011, **12**, 237–268.
59 R. Abe, *J. Photochem. Photobiol., C*, 2010, **11**, 179–209.
60 K. Wu, H. Zhu, Z. Liu, W. Rodríguez-Córdoba and T. Lian, *J. Am. Chem. Soc.*, 2012, **134**, 10337–10340.
61 H.-Y. Lin, H.-C. Yang and W.-L. Wang, *Catal. Today*, 2011, **174**, 106–113.
62 S. Ida and T. Ishihara, *J. Phys. Chem. Lett.*, 2014, **5**, 2533–2542.
63 X. Zhang, K.-A. Min, W. Zheng, J. Hwang, B. Han and L. Y. S. Lee, *Appl. Catal., B*, 2020, **273**, 118927.
64 J. Ran, H. Zhang, S. Fu, M. Jaroniec, J. Shan, B. Xia, Y. Qu, J. Qu, S. Chen, L. Song, J. M. Cairney, L. Jing and S.-Z. Qiao, *Nat. Commun.*, 2022, **13**, 4600.
65 T. A. Shifa, F. Wang, Z. Cheng, P. He, Y. Liu, C. Jiang, Z. Wang and J. He, *Adv. Funct. Mater.*, 2018, **28**, 1800548.
66 X. Zhang, X. Zhao, D. Wu, Y. Jing and Z. Zhou, *Adv. Sci.*, 2016, **3**, 1600062.
67 J. Yang, Y. Zhou, Q. Guo, Y. Dedkov and E. Voloshina, *RSC Adv.*, 2020, **10**, 851–864.
68 J. Liu, X.-B. Li, D. Wang, W.-M. Lau, P. Peng and L.-M. Liu, *J. Chem. Phys.*, 2014, **140**, 054707.
69 C.-F. Du, Q. Liang, R. Dangol, J. Zhao, H. Ren, S. Madhavi and Q. Yan, *Nano-Micro Lett.*, 2018, **10**, 67.
70 K.-z. Du, X.-z. Wang, Y. Liu, P. Hu, M. I. B. Utama, C. K. Gan, Q. Xiong and C. Kloc, *ACS Nano*, 2016, **10**, 1738–1743.
71 Y. Zhang, Y. Zhao, C. Bao, Y. Xiao, Y. Xiang, M. Song, W. Huang, L. Ma, H. Hou and X. Chen, *J. Alloys Compd.*, 2022, **909**, 164731.
72 T. A. Shifa, F. Wang, Z. Cheng, P. He, Y. Liu, C. Jiang, Z. Wang and J. He, *Adv. Funct. Mater.*, 2018, **28**, 1800548.
73 K. Chen, J. Liu, Z. Huang, S. Zong, L. Liu and W. Tan, *Int. J. Hydrogen Energy*, 2021, **46**, 33823–33834.
74 F. Wang, T. A. Shifa, P. Yu, P. He, Y. Liu, F. Wang, Z. Wang, X. Zhan, X. Lou, F. Xia and J. He, *Adv. Funct. Mater.*, 2018, **28**, 1802151.
75 R. Brec, *Solid State Ion.*, 1986, **22**, 3–30.
76 G. Kliche, *Z. Naturforsch. A*, 1983, **38**, 1133–1137.
77 J. Banys, J. Macutkevic, R. Grigalaitis and J. Vysochanskii, *Solid State Ionics*, 2008, **179**, 79–81.
78 B. Zapeka, M. Kostyrko, I. Martynyuk-Lototska and R. Vlokh, *Philos. Mag.*, 2015, **95**, 382–393.
79 R. Samal, G. Sanyal, B. Chakraborty and C. S. Rout, *J. Mater. Chem. A*, 2021, **9**, 2560–2591.
80 A. Wiedenmann, J. Rossat-Mignod, A. Louisy, R. Brec and J. Rouxel, *Solid State Commun.*, 1981, **40**, 1067–1072.
81 S. Joergens and A. Mewis, *Z. fur Anorg. Allg. Chem.*, 2004, **630**, 51–57.
82 S. Lee, P. Colombet, G. Ouvrard and R. Brec, *Inorg. Chem.*, 1988, **27**, 1291–1294.
83 Z. Ouili, A. Leblanc and P. Colombet, *J. Solid State Chem.*, 1987, **66**, 86–94.
84 G. Burr, E. Durand, M. Evain and R. Brec, *J. Solid State Chem.*, 1993, **103**, 514–518.
85 R. Pfeiff and R. Kniep, *Z. fur Naturforsch. – B*, 1993, **48**, 1270–1274.
86 A. I. Brusilovets and T. I. Fedoruk, *Zhurnal Neorganicheskoj Khimii*, 1977, **22**, 2085–2087.
87 P. Vishnoi, K. Pramoda and C. N. R. Rao, *ChemNanoMat*, 2019, **5**, 1062–1091.
88 K. Singh, A. Ohlan and S. Dhawan, *Nanocompos.: New Trends Dev.*, 2012, DOI: **10.5772/50408**.
89 S. Lee, K.-Y. Choi, S. Lee, B. H. Park and J.-G. Park, *APL Mater.*, 2016, **4**, 086108.
90 W. Zhu, W. Gan, Z. Muhammad, C. Wang, C. Wu, H. Liu, D. Liu, K. Zhang, Q. He, H. Jiang, X. Zheng, Z. Sun, S. Chen and L. Song, *Chem. Commun.*, 2018, **54**, 4481–4484.
91 K. Synnatschke, S. Shao, J. van Dinter, Y. J. Hofstetter, D. J. Kelly, S. Grieger, S. J. Haigh, Y. Vaynzof, W. Bensch and C. Backes, *Chem. Mater.*, 2019, **31**, 9127–9139.
92 X. Li, Y. Fang, J. Wang, B. Wei, K. Qi, H. Y. Hoh, Q. Hao, T. Sun, Z. Wang, Z. Yin, Y. Zhang, J. Lu, Q. Bao and C. Su, *Small*, 2019, **15**, 1902427.
93 M. Barua, M. M. Ayyub, P. Vishnoi, K. Pramoda and C. N. R. Rao, *J. Mater. Chem. A*, 2019, **7**, 22500–22506.
94 D. Rakov, Y. Li, S. Niu and P. Xu, *J. Alloys Compd.*, 2018, **769**, 532–538.
95 F. Liu, L. You, K. L. Seyler, X. Li, P. Yu, J. Lin, X. Wang, J. Zhou, H. Wang, H. He, S. T. Pantelides, W. Zhou, P. Sharma, X. Xu, P. M. Ajayan, J. Wang and Z. Liu, *Nat. Commun.*, 2016, **7**, 12357.

96 B. Song, K. Li, Y. Yin, T. Wu, L. Dang, M. Cabán-Acevedo, J. Han, T. Gao, X. Wang, Z. Zhang, J. R. Schmidt, P. Xu and S. Jin, *ACS Catal.*, 2017, **7**, 8549–8557.
97 Y. Sun, A. Huang, Z. Li, Y.-Q. Fu and Z. Wang, *Electrocatalysis*, 2022, **13**, 494–501.
98 C. C. Mayorga-Martinez, Z. Sofer, D. Sedmidubský, Š. Huber, A. Y. S. Eng and M. Pumera, *ACS Appl. Mater. Interfaces*, 2017, **9**, 12563–12573.
99 B. H. R. Suryanto, Y. Wang, R. K. Hocking, W. Adamson and C. Zhao, *Nat. Commun.*, 2019, **10**, 5599.
100 Z. P. Ifkovits, J. M. Evans, M. C. Meier, K. M. Papadantonakis and N. S. Lewis, *Energy Environ. Sci.*, 2021, **14**, 4740–4759.
101 P. J. McHugh, A. D. Stergiou and M. D. Symes, *Adv. Energy Mater.*, 2020, **10**, 2002453.
102 C. N. R. Rao and M. Chhetri, *Adv. Mater.*, 2019, **31**, 1803668.
103 M. M. Ayyub, M. Chhetri, U. Gupta, A. Roy and C. N. R. Rao, *Chem. – Eur. J.*, 2018, **24**, 18455–18462.
104 L. Feng, H. Vrubel, M. Bensimon and X. Hu, *Phys. Chem. Chem. Phys.*, 2014, **16**, 5917–5921.
105 J. Wang, X. Li, B. Wei, R. Sun, W. Yu, H. Y. Hoh, H. Xu, J. Li, X. Ge, Z. Chen, C. Su and Z. Wang, *Adv. Funct. Mater.*, 2020, **30**, 1908708.
106 R. N. Jenjeti, M. P. Austeria and S. Sampath, *ChemElectroChem*, 2016, **3**, 1392–1399.
107 R. Wang, J. Huang, X. Zhang, J. Han, Z. Zhang, T. Gao, L. Xu, S. Liu, P. Xu and B. Song, *ACS Nano*, 2022, **16**, 3593–3603.
108 Megha and P. Sen, *Int. J. Hydrogen Energy*, 2023, **48**, 21778–21787.
109 C. Tang, D. He, N. Zhang, X. Song, S. Jia, Z. Ke, J. Liu, J. Wang, C. Jiang, Z. Wang, X. Huang and X. Xiao, *Energy Environ. Mater.*, 2022, **5**, 899–905.
110 Q. Liang, L. Zhong, C. Du, Y. Luo, J. Zhao, Y. Zheng, J. Xu, J. Ma, C. Liu, S. Li and Q. Yan, *ACS Nano*, 2019, **13**, 7975–7984.
111 M. G. Sendeku, F. Wang, Z. Cheng, P. Yu, N. Gao, X. Zhan, Z. Wang and J. He, *ACS Appl. Mater. Interfaces*, 2021, **13**, 13392–13399.
112 Y. Zhao, C. Bao, Y. Zhang, K. Du, W. Huang and C. Su, *Mater. Lett.*, 2022, **324**, 132687.
113 F. Wang, T. A. Shifa, P. He, Z. Cheng, J. Chu, Y. Liu, Z. Wang, F. Wang, Y. Wen, L. Liang and J. He, *Nano Energy*, 2017, **40**, 673–680.
114 Q. Pei, Y. Song, X. Wang, J. Zou and W. Mi, *Sci. Rep.*, 2017, **7**, 9504.
115 J. Ran, H. Zhang, S. Fu, M. Jaroniec, J. Shan, B. Xia, Y. Qu, J. Qu, S. Chen, L. Song, J. M. Cairney, L. Jing and S.-Z. Qiao, *Nat. Commun.*, 2022, **13**, 4600.
116 B. Xia, B. He, J. Zhang, L. Li, Y. Zhang, J. Yu, J. Ran and S.-Z. Qiao, *Adv. Energy Mater.*, 2022, **12**, 2201449.
117 S. Kim, N. T. Nguyen and C. W. Bark, *Appl. Sci.*, 2018, **8**, 1526.
118 Y. Li, J. Li, W. Yang and X. Wang, *Nanoscale Horiz.*, 2020, **5**, 1174–1187.
119 S. Huang, Z. Shuai and D. Wang, *J. Mater. Chem. A*, 2021, **9**, 2734–2741.
120 B. Lin, A. Chaturvedi, J. Di, L. You, C. Lai, R. Duan, J. Zhou, B. Xu, Z. Chen, P. Song, J. Peng, B. Ma, H. Liu, P. Meng, G. Yang, H. Zhang, Z. Liu and F. Liu, *Nano Energy*, 2020, **76**, 104972.
121 X. Ren, C. Tang, B. Xu, W. Tang, B. Lin and G. Yang, *Mater. Lett.*, 2023, **333**, 133654.
122 S. Gupta, M. K. Patel, A. Miotello and N. Patel, *Adv. Funct. Mater.*, 2020, **30**, 1906481.
123 C. C. Mayorga-Martinez, Z. Sofer, D. Sedmidubský, Š. Huber, A. Y. S. Eng and M. Pumera, *ACS Appl. Mater. Interfaces*, 2017, **9 14**, 12563–12573.
124 R. Gusmão, Z. Sofer and M. Pumera, *Adv. Funct. Mater.*, 2019, **29**, 1805975.
125 N. Coleman, I. A. Liyanage, M. D. Lovander, J. leddy and E. G. gillan, *Molecules*, 2022, **27**, 5053.
126 J. Luxa, Š. Cintl, L. Spejchalová, J.-Y. Lin and Z. Sofer, *ACS Appl. Energy Mater.*, 2020, **3**, 11992–11999.
127 H. Zhang, G. Qi, W. Liu, S. Zhang, Q. Liu, J. Luo and X. Liu, *Inorg. Chem. Front.*, 2023, **10**, 2423–2429.
128 M. Sial, H. Lin and X. Wang, *Nanoscale*, 2018, **10**, 12975–12980.
129 L. Fang, Y. Xie, P. Guo, J. Zhu, S. Xiao, S. Sun, W. Zi and H. Zhao, *Sustainable Energy Fuels*, 2021, **5**, 2537–2544.
130 Q. Liang, L. Zhong, C. Du, Y. Zheng, Y. Luo, J. Xu, S. Li and Q. Yan, *Adv. Funct. Mater.*, 2018, **28**, 1805075.
131 Z. Cheng, M. Getaye and Q. Liu, *Nanotechnology*, 2019, 31.
132 J. Zhang, F. Feng, Y. Pu, X. Li, C. H. Lau and W. Huang, *ChemSusChem*, 2019, **12**, 2651–2659.
133 Z. Cheng, T. A. Shifa, F. Wang, Y. Gao, P. He, K. Zhang, C. Jiang, Q. Liu and J. He, *Adv. Mater.*, 2018, **30**, 1707433.
134 H. Li, N. Wells, B. Chong, B. Xu, J. Wei, B. Yang and Y. Guidong, *Chem. Eng. Sci.*, 2020, **229**, 116069.
135 M. G. Sendeku, F. Wang, Z. Cheng, P. Yu, N. Gao, X. Zhan, Z. Wang and J. He, *ACS Appl. Mater. Interfaces*, 2021, **13**(11), 13392–13399.
136 K. Chen, J. Liu, Z. Huang, S. Zong, L. Liu, W. Tan and Y. Fang, *J. Colloid Interface Sci.*, 2022, **627**, 438–448.
137 P. Yang, H. Ou, Y. Fang and X. Wang, *Angew. Chem., Int. Ed.*, 2017, **56**, 3992–3996.
138 L. Wang, Y. Hu, J. Xu, Z. Huang, H. Lao, X. Xu, J. Xu, H. Tang, R. Yuan, Z. Wang and Q. Liu, *Int. J. Hydrogen Energy*, 2023, **48**, 16987–16999.
139 P. Hu, C. K. Ngaw, Y. Yuan, P. S. Bassi, S. C. Joachim Loo and T. T. Yang Tan, *Nano Energy*, 2016, **26**, 577–585.
140 X. Chen, Y. Guo, R. Bian, Y. Ji, X. Wang, X. Zhang, H. Cui and J. Tian, *J. Colloid Interface Sci.*, 2022, **613**, 644–651.
141 J. Jia, W. Sun, Q. Zhang, X. Zhang, X. Hu, E. Liu and J. Fan, *Appl. Catal., B*, 2020, **261**, 118249.
142 Y. Mi, L. Wen, Z. Wang, D. Cao, R. Xu, Y. Fang, Y. Zhou and Y. Lei, *Nano Energy*, 2016, **30**, 109–117.
143 X. Zhu, T. Zhang, Z. Sun, H. Chen, J. Guan, X. Chen, H. Ji, P. Du and S. Yang, *Adv. Mater.*, 2017, **29**, 1605776.
144 J. Xu and X. Cao, *Chem. Eng. J.*, 2015, **260**, 642–648.
145 B. Ma, P.-Y. Guan, Q.-Y. Li, M. Zhang and S.-Q. Zang, *ACS Appl. Mater. Interfaces*, 2016, **8**, 26794–26800.

146 Y.-J. Yuan, Z. Shen, S. Wu, Y. Su, L. Pei, Z. Ji, M. Ding, W. Bai, Y. Chen, Z.-T. Yu and Z. Zou, *Appl. Catal., B*, 2019, **246**, 120–128.
147 S. Masimukku, D.-L. Tsai, Y.-T. Lin, I. L. Chang and J.-J. Wu, *Appl. Surf. Sci.*, 2023, **614**, 156147.
148 R. Chen, H. Zhou, C. Han, P. Wang, R. Wang, Z. Liu, X. Ma and Y. Huang, *ACS Appl. Energy Mater.*, 2022, **5**, 12897–12906.
149 B. Archana, N. Kottam, S. Nayak, K. B. Chandrasekhar and M. B. Sreedhara, *J. Phys. Chem. C*, 2020, **124**, 14485–14495.
150 C. Peng, T. Zhou, P. Wei, H. Ai, B. Zhou, H. Pan, W. Xu, J. Jia, K. Zhang, H. Wang and H. Yu, *Chem. Eng. J.*, 2022, **439**, 135685.
151 Y. Wang, C. Zeng, L. Wu, Y. Dong, Y. Zhang, D. Yang, W. Hu, J. Hao, H. Pan and R. Yang, *J. Mater. Sci. Technol.*, 2023, **146**, 113–120.